

REVIEWS OF TOPICAL PROBLEMS

PACS numbers: **12.38.–t**, 12.39.St, **13.87.–a**

QCD and the physics of hadronic collisions

M L Mangano

DOI: 10.3367/UFNe.0180.201002a.0113

Contents

Abstract. We review the basic principles underlying the use of quantum chromodynamics in understanding the structure of high-Q^2 processes in high-energy hadronic collisions. Several applications relevant to the Tevatron and the LHC are illustrated.

1. Introduction

The frontier of high-energy physics will soon be redefined by experiments at CERN's Large Hadron Collider (LHC), the proton–proton collider operating at the center-of-mass energy 14 TeV. The main goal of these experiments is to unveil the nature of electroweak symmetry breaking via the detection of the Higgs boson and of other new particles associated with possible extensions of the Standard Model (SM). Strong interactions between quarks and gluons, described by quantum chromodynamics (QCD), have no direct relation to electroweak phenomena, but their role in making the LHC physics program possible cannot be underestimated. The processes leading to the creation of Higgs bosons and other interesting particles are all driven by the interactions among quarks and gluons, and these interactions will define the production rate of new phenomena, as well as of the numerous SM processes that will act as irreducible backgrounds to their detection. A solid and quantitative understanding of the role of strong interactions in LHC physics is therefore essential for a full exploitation of the LHC potential. Most of the collisions between protons are the result of the complex long-distance QCD responsible for holding quarks together, and their quantitative description still lacks a robust first-principle understanding. On the other hand, the processes leading to the production of heavy elementary particles arise from short-distance interactions among point-like proton constituents. These *hard* interactions can be described by the perturbative regime of QCD, making it possible to perform quantitative, first-principle predictions.

This review illustrates the basic principles underlying the use of perturbative QCD in predicting the structure of hard processes in high-energy hadronic collisions. The starting point, in Section 2, is a discussion of the factorization formula, which is the basis for the description of all hard processes in terms of universal functions parameterizing the density of quarks and gluons inside the proton. In Section 3, we discuss the evolution of perturbative final states, made up of quarks and gluons, toward physical systems made of hadrons. Finally, Section 4 collects several applications and examples of comparisons between theoretical predictions and the current data from the Fermilab Tevatron ($p\bar{p}$) collider. These provide a picture of the success of this theoretical framework, giving good confidence in the reliability of its future applications to the study of LHC collisions.

The treatment is introductory, and the emphasis is placed on basic and intuitive physics concepts. Given the large number of papers that have contributed to the development of the field, it is impossible to provide a complete and fair bibliography. We therefore limit the bibliography to some review books and to references to some of the key results discussed here. For an excellent description of the early ideas about quarks and their dynamics, the classic reference is Feynman's book [1]. The emergence of QCD as a theory for strong interactions is nicely reviewed in [2]. For a general, but rather formal, introduction to QCD, see, e.g., Ref. [3]. For a more modern and pedagogical introduction, in the context of an introductory course to field theory, we refer to the

M L Mangano Theory Group, PH Department, CERN, Geneva, Switzerland

Received 8 June, revised 7 September 2009
Uspekhi Fizicheskikh Nauk **180** (2) 113 – 138 (2010)
DOI: 10.3367/UFNr.0180.201002a.0113
Translated by O V Teryaev; edited by A M Semikhatov

excellent book by Peskin and Schröder [4]. For a general introduction to collider physics, see Ref. [5]. For QCD applications to the LEP, Tevatron, and LHC, see Ref. [6] and, specifically for the LHC, Ref. [7]. Explicit calculations, including the subtle details of next-to-leading-order (NLO) calculations and renormalization, are given in great detail for several concrete cases of interest in Ref. [8]. Many of the ideas used in this review are inspired by the very physical perspective presented in Ref. [9]. We make occasional reference to perturbative calculations and to Monte Carlo generator tools, but do not provide a systematic review of the state of the art in these very active areas. For recent status reports, see [10, 11].

2. QCD and the proton structure at large Q^2

The understanding of the structure of the proton at short distances is one of the key ingredients to predicting cross sections for processes involving hadrons in the initial state. All processes in hadronic collisions, even those of an intrinsically electroweak nature such as the production of W/Z bosons or photons, are in fact induced by the quarks and gluons contained inside the hadron. In this section, we introduce some important concepts, such as the notion of partonic densities of the proton, and of parton evolution. These are the essential tools used by theorists to predict production rates for hadronic reactions.

We limit ourselves to processes where a proton–(anti)proton pair collides at a large center-of-mass energy ($\sqrt{S}$, typically larger than several hundred GeV) and undergoes a very inelastic interaction, with momentum transfers between the participants in excess of several GeV. The outcome of this hard interaction could be the simple scattering at a large angle of some of hadron's elementary constituents, their annihilation into new massive resonances, or a combination of the two possibilities. In all cases, the final state consists of a large multiplicity of particles associated with the evolution of the fragments of the initial hadrons, as well as of the new states produced. As discussed below, the fundamental physical concept that makes the theoretical description of these phenomena possible is 'factorization,' namely, the ability to isolate separate independent phases of the overall collision. These phases are dominated by different dynamics, and the most appropriate techniques can be applied to describe each of them separately. In particular, factorization allows decoupling the complexity of the proton structure and of the final-state hadron formation from the elementary nature of the perturbative hard interaction among the partonic constituents.

Figure 1 illustrates how this works. As the left proton travels freely before coming into contact with the hadron coming in from the right, its constituent quarks are held together by the constant exchange of virtual gluons (e.g., gluons a and b in Fig. 1). These gluons are mostly soft, because any hard exchange would cause the constituent quarks to fly apart, and a second hard exchange would be necessary to reestablish the balance of momentum and keep the proton together. Gluons of high virtuality (gluon c in Fig. 1) therefore prefer to be reabsorbed by the same quark within a time inversely proportional to their virtuality, as prescribed by the uncertainty principle. But the state of the quark is left unchanged by this process. Altogether, this suggests that the global state of the proton, although defined by a complex set of gluon exchanges between quarks, is

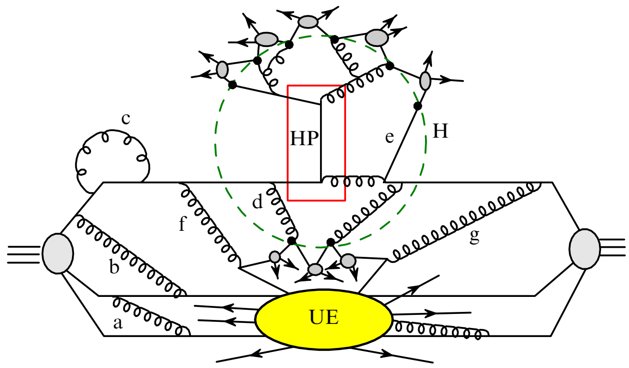

Figure 1. General structure of a hard proton–proton collision.

nevertheless determined by interactions that have a time scale of the order of $1/m_{\mathrm{p}}$. When seen in the laboratory frame where the proton is moving with the energy $\sqrt{s}/2$, this time is furthermore Lorentz-dilated by the factor $\gamma = \sqrt{s}/2m_{\mathrm{p}}$. If we disturb a quark with a probe of virtuality $Q \gg m_{\mathrm{p}}$, the time frame for this interaction is so short $(1/Q)$ that the interactions of the quark with the rest of the proton can be neglected. The struck quark cannot negotiate a coherent response to the external perturbation with its partners: it simply does not have the time to communicate to them that it is being kicked away. On this time scale, only gluons with an energy of the order of Q can be emitted, something which, to happen coherently over the whole proton, is suppressed by powers of m_{p}/Q (this suppression characterizes the 'elastic form factor' of the proton). In the figure, the hard process is represented by the rectangle labeled HP. In this example, a head-on collision with a gluon from the opposite hadron leads to a $\mathrm{qg} \to \mathrm{qg}$ scattering with a momentum exchange of the order of Q. This and other possible processes can be calculated from first principles in perturbative QCD, using elementary quarks and gluons as external states.

When a constituent is suddenly deflected, the partons that it has recently radiated cannot be reabsorbed (as happened to gluon c earlier) because the constituent is no longer there waiting for the partons to return. This is the case, for example, of the gluon d emitted by the quark, and of the quark e from the opposite hadron; the emitted gluon is engaged in the hard interaction. The number of 'liberated' partons depends on the hard scale Q: the larger the value of Q is, the more sudden the deflection of the struck parton, and the fewer are the partons that can reconnect before its departure (typically only partons with a virtuality larger than Q).

After the hard process, the partons liberated during the evolution prior to the collision and the partons created by the hard collision also emit radiation. The radiation process, governed by perturbative QCD, continues until a low-virtuality scale is reached (the boundary region labeled with the dotted line, H, in Fig. 1). To describe this perturbative evolution phase, proper care has to be taken to incorporate quantum coherence effects, which in principle connect the probabilities of radiation of different partons in the event. Once the low-virtuality scale is reached, the memory of the hard-process phase is lost, once again as a result of different time scales in the problem, and the final phase of hadronization takes over. Because of the decoupling from the hard-process phase, the hadronization is assumed to be independent of the initial hard process, and its parameterization, tuned to the observables of some reference process, can then be used in other hard interactions (universality of hadronization). Nearby partons merge into color-singlet clusters (the grey blobs in Fig. 1), which then decay phenomenologically into physical hadrons. To complete the picture, we need to understand the evolution of the fragments of the initial hadrons. As shown in Fig. 1, this evolution cannot be entirely independent of what happens in the hard event, because color quantum numbers must at least be exchanged to guarantee the overall neutrality and baryon number conservation. In our example, gluons f and g, emitted early on in the perturbative evolution of the initial state, split into $q\bar{q}$ pairs that are shared between the hadron fragments (whose overall interaction is represented by the oval labeled UE, for underlying event) and the clusters resulting from the evolution of the initial state.

The above ideas are embodied in the following factorization formula, which represents the starting point of any theoretical analysis of cross sections and observables in hadronic collisions:

$$\frac{\mathrm{d}\sigma}{\mathrm{d}X} = \sum_{j,k} \int_{\hat{X}} f_j(x_1, Q) f_k(x_2, Q)\, \frac{\mathrm{d}\hat{\sigma}_{jk}(Q)}{\mathrm{d}\hat{X}}\, F(\hat{X} \to X;\, Q)\,, \tag{1}$$

where X is some hadronic observable (e.g., the transverse momentum of a pion, the invariant mass of a combination of particles); the summation over j and k ranges over the parton types inside the colliding hadrons; the function $f_j(x, Q)$ (known as the parton distribution function, PDF) parameterizes the number density of parton type j with the momentum fraction x in a proton probed at a scale Q (the meaning of this scale is discussed in more detail below); $\hat{X}$ is a parton-level kinematical variable (e.g., the transverse momentum of a parton from the hard scattering); $\hat{\sigma}_{jk}$ is the parton-level cross section, differential in the variable $\hat{X}$; $F(\hat{X} \to X;\, Q)$ is a transition function, weighing the probability that the partonic state defining $\hat{X}$ gives rise to the hadronic observable X after hadronization.

In the rest of this section, we cover the above ideas in some more detail. We do not provide a rigorous proof of the legitimacy of this approach, but try to justify it qualitatively to make it sound at least plausible.

2.1 Parton densities and their evolution

As mentioned above, the binding forces responsible for quark confinement are due to the exchange of rather soft gluons. If a quark were to exchange just a single hard virtual gluon with another quark, the recoil would tend to break the proton apart. It is easy to verify that the exchange of gluons with a virtuality larger than Q is then proportional to some large power of m_p/Q, m_p being the proton mass. Since the gluon coupling constant decreases at large Q, exchange of hard gluons is significantly suppressed.[1] We consider the picture in Fig. 2. The exchange of two gluons is required to ensure that the momentum exchanged after the first gluon emission is returned to the quark, and the proton maintains its structure. The contributions of hard gluons to this process can be approximated by integrating the loop over large

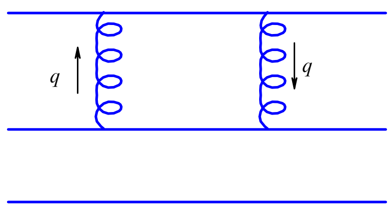

Figure 2. Gluon exchange inside a proton.

momenta:

$$\int_Q \frac{\mathrm{d}^4 q}{q^6} \sim \frac{1}{Q^2}\,. \tag{2}$$

At large Q, this contribution is suppressed by powers of $(m_\mathrm{p}/Q)^2$, where the proton mass m_p is included as being the only dimensional quantity available (the fundamental QCD scale Λ_QCD could also be used here, but numerically this is of the order of a GeV anyway). The interactions keeping the proton together are therefore dominated by soft exchanges, with a virtuality Q of the order of m_p. Owing to Heisenberg's uncertainty principle, the typical time scale of these exchanges is of the order of $1/m_\mathrm{p}$: this is the time during which fluctuations with a virtuality of the order of m_p can survive. In the laboratory system, where the proton travels with an energy E, this time is Lorentz-dilated to $\tau \sim \gamma/m_\mathrm{p} = E/m_\mathrm{p}^2$. If we probe the proton with an off-shell photon, the interaction takes place during the limited lifetime of the virtual photon, which, again due to the uncertainty principle, is given by the inverse of its virtuality. Assuming the virtuality $Q \gg m_\mathrm{p}$, once the photon is 'inside' the proton and meets a quark, the struck quark has no time to negotiate a coherent response with the other quarks, because the time scale for it to 'talk' to its partners is too long compared with the duration of the interaction with the photon itself. As a result, the struck quark has no option but to interact with the photon as if it were a free particle.

We consider in more detail what happens during such a process. In Fig. 3, we see a proton as it approaches a hard collision with a photon of virtuality Q. Gluons emitted at a scale $q > Q$ have time to be reabsorbed, since their lifetime is very short. Their contribution to the process can be calculated in perturbative QCD, because the scale is large in the domain where perturbative calculations are meaningful. After the quark is reabsorbed, its state remains the same, the only effect being an overall renormalization of the wave function, which does not affect the quark density. But a gluon emitted at a scale $q < Q$ has a lifetime longer than the time it takes for the quark to interact with the photon, and by the time it tries to reconnect to its parent quark, the quark has been kicked away

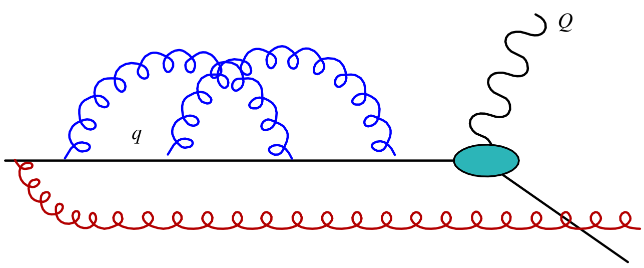

Figure 3. Gluon emission at different scales during the approach to a hard collision.

[1] The fact that the coupling decreases at large Q plays a fundamental role in this argument. Were this not true, the parton picture could not be used!

by the photon, and is no longer there. Because the gluon has taken away some of the quark momentum, the momentum fraction x of the quark as it enters the interaction with the photon is different from the momentum it had before, and therefore its density $f(x)$ is affected. Furthermore, when the scale q is of the order of 1 GeV, the state of the quark is not calculable in perturbative QCD. This state depends on the internal wave function of the proton, which cannot be predicted in perturbative QCD. We can, however, say that the wave function of the proton, and therefore the state of the 'free' quark, is determined by the dynamics of the soft-gluon exchanges inside the proton itself. Because the time scale of these dynamics is long relative to the time scale of the photon–quark interaction, we can safely argue that to good approximation, the photon sees a static snapshot of the proton inner configuration. In other words, the state of the quark had been prepared long before the photon arrived. This also suggests that the state of the quark is independent of the precise nature of the external probe under the condition that the time scale of the hard interaction is very short compared to the time it would take for the quark to readjust itself. As a result, if we could perform some measurement of the quark state, e.g., using a virtual-photon probe, we could then use this knowledge of the state of the quark to perform predictions for the interaction of the proton with any other probe (e.g., a virtual W boson or even a gluon from an opposite beam of hadrons). This is the essence of the universality of the parton distributions.

The above picture leads to an important observation. It turns out that the distinction between gluons that are reabosrbed and those that are not depends on the scale Q of the hard probe. As a result, the parton density $f(x)$ turns out to depend on Q. This is illustrated in Fig. 4.

The gluon emitted at a scale μ has a lifetime short enough to be reabsorbed before a collision with a photon of a virtuality $Q < \mu$, but too long for a photon of a virtuality $Q > \mu$. The partonic density $f(x)$ therefore changes in passing from μ to Q. We can easily describe this variation as

$$f(x,Q) = f(x,\mu) + \int_x^1 \mathrm{d}x_{\mathrm{in}} f(x_{\mathrm{in}},\mu) \int_\mu^Q \mathrm{d}q^2 \times \int_0^1 \mathrm{d}y\, \mathcal{P}(y,q^2)\, \delta(x - y x_{\mathrm{in}}) \,. \tag{3}$$

Here, we obtain the density at the scale Q as the sum of $f(x)$ at the scale μ [which we label as $f(x,\mu)$] and the contribution of all the quarks with momentum $x_{\mathrm{in}} > x$ that retain a proton-momentum fraction $x = y x_{\mathrm{in}}$ by emitting a gluon. The function $\mathcal{P}(y,Q^2)$ describes the 'probability' of the quark emitting a gluon at a scale Q, keeping the fraction y of its momentum. This function is independent of the details of the hard process, and simply describes the radiation of a free quark subject to an interaction with a virtuality Q. Since $f(x,Q)$ is independent of μ (μ is just used as a reference scale to construct our argument), the total derivative of the right-hand side with respect to μ must vanish, leading to the equation

$$\frac{\mathrm{d}f(x,Q)}{\mathrm{d}\mu^2} = 0 \quad \Rightarrow \frac{\mathrm{d}f(x,\mu)}{\mathrm{d}\mu^2} = \int_x^1 \frac{\mathrm{d}y}{y} f(y,\mu)\, \mathcal{P}\left(\frac{x}{y},\, \mu^2\right). \tag{4}$$

Dimensional analysis and the fact that the gluon emission rate is proportional to the QCD coupling squared allow us to further write

$$\mathcal{P}(x,Q^2) = \frac{\alpha_{\mathrm{s}}}{2\pi} \frac{1}{Q^2} P(x) \,, \tag{5}$$

from which the Dokshitzer–Gribov–Lipatov–Altarelli–Parisi (DGLAP) equation follows [12–14]:

$$\frac{\mathrm{d}f(x,\mu)}{\mathrm{d}\log\mu^2} = \frac{\alpha_{\mathrm{s}}}{2\pi} \int_x^1 \frac{\mathrm{d}y}{y} f(y,\mu)\, P_{\mathrm{qq}}\left(\frac{x}{y}\right). \tag{6}$$

The so-called *splitting function* $P_{\mathrm{qq}}(x)$ can be calculated in perturbative QCD. The subscript qq is a labeling convention indicating that x refers to the momentum fraction retained by a quark after the emission of a gluon.

More generally, we should consider additional processes, for example, the cases where the quark interacting with the photon comes from the splitting of a gluon. This is shown in Fig. 5: the left diagram is the one we considered above; the right diagram corresponds to processes where an emitted gluon has the time to split into a $q\bar{q}$ pair, and one of these quarks interacts with the photon. The overall evolution equation, including the effect of gluon splitting, is given by

$$\frac{\mathrm{d}q(x,Q)}{\mathrm{d}t} = \frac{\alpha_{\mathrm{s}}}{2\pi} \int_x^1 \frac{\mathrm{d}y}{y} \left[q(y,Q)\, P_{\mathrm{qq}}\left(\frac{x}{y}\right) + g(y,Q)\, P_{\mathrm{qg}}\left(\frac{x}{y}\right) \right], \tag{7}$$

where $t = \log Q^2$.

For external probes that couple to gluons (for example, an external gluon, coming, for instance, from an incoming proton), we have a similar evolution of the gluon density (see Fig. 6):

$$\frac{\mathrm{d}g(x,Q)}{\mathrm{d}t} = \frac{\alpha_{\mathrm{s}}}{2\pi} \int_x^1 \frac{\mathrm{d}y}{y} \left[g(y,Q)\, P_{\mathrm{gg}}\left(\frac{x}{y}\right) + \sum_{q,\bar{q}} q(y,Q)\, P_{\mathrm{gq}}\left(\frac{x}{y}\right) \right]. \tag{8}$$

At the leading order (LO) of the perturbation theory, the explicit calculation of the splitting functions $P_{ij}(x)$ (see, e.g.,

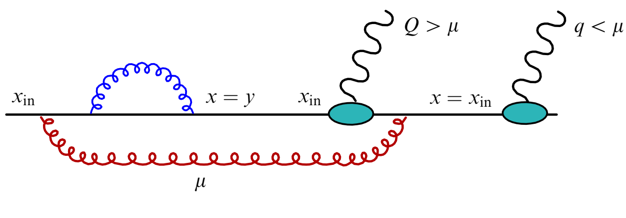

Figure 4. Scale dependence of the gluon emission during a hard collision.

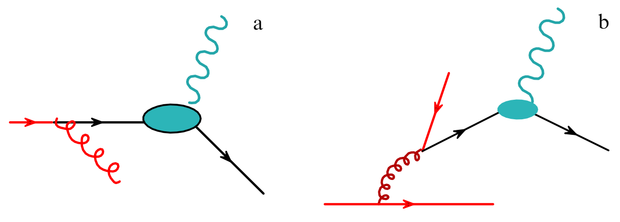

Figure 5. The processes leading to the evolution of the quark density.

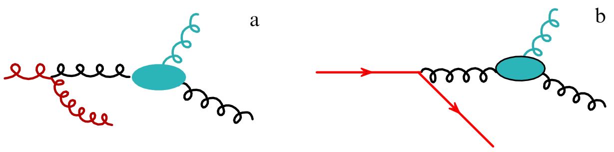

Figure 6. The processes leading to the evolution of the gluon density.

Ref. [8]) then gives the expressions [2]

$$P_{\mathrm{qq}}(x) = P_{\mathrm{gq}}(1-x) = C_{\mathrm{F}}\,\frac{1+x^2}{1-x}\,, \tag{9}$$

$$P_{\mathrm{qg}}(x) = \frac{1}{2}\left[x^2 + (1-x)^2\right], \tag{10}$$

$$P_{\mathrm{gg}}(x) = 2C_{\mathrm{A}}\left[\frac{1-x}{x} + \frac{x}{1-x} + x(1-x)\right], \tag{11}$$

where $x \neq 1$ and $C_{\mathrm{A}} = 2N_{\mathrm{c}}$ are the Casimir invariants of the fundamental and adjoint representation of $\mathrm{SU}(N_{\mathrm{c}})$ ($N_{\mathrm{c}} = 3$ for QCD). In what follows, we derive some general properties of the PDF evolution and give several concrete examples.

The factorization given by Eqn (1) cannot of course hold for all phenomena in hadronic collisions. Processes like elastic scattering or generic soft collisions cannot be described in terms of quarks and gluons because they are driven by the long-distance structure of the proton. Furthermore, modifications of this simple factorization relation can be required to describe processes like hard diffraction. The DGLAP evolution of parton densities, furthermore, requires modifications with respect to what is shown here when x is so small that $\alpha_{\mathrm{s}} \log 1/x$ is of the order of unity, or when the gluon density becomes so large that gluon recombination becomes possible. Since the processes we consider in our applications do not cover these cases, we do not further discuss these aspects in this review.

2.2 General properties of parton density evolution

Defining the moments of an arbitrary function $g(x)$ as

$$g_n = \int_0^1 \frac{\mathrm{d}x}{x}\, x^n\, g(x)\,,$$

it is easy to prove that the evolution equations for the moments turn into ordinary linear differential equations:

$$\frac{\mathrm{d}f_{\mathrm{i}}^{(n)}}{\mathrm{d}t} = \frac{\alpha_{\mathrm{s}}}{2\pi}\left[P_{\mathrm{qq}}^{(n)} f_{\mathrm{i}}^{(n)} + P_{\mathrm{qg}}^{(n)} f_{\mathrm{g}}^{(n)}\right], \tag{12}$$

$$\frac{\mathrm{d}f_{\mathrm{g}}^{(n)}}{\mathrm{d}t} = \frac{\alpha_{\mathrm{s}}}{2\pi}\left[P_{\mathrm{gg}}^{(n)} f_{\mathrm{g}}^{(n)} + P_{\mathrm{gq}}^{(n)} f_{\mathrm{i}}^{(n)}\right]. \tag{13}$$

It is convenient to introduce the *valence* $V(x,t)$ and *singlet* $\Sigma(x,t)$ densities:

$$V(x) = \sum_i f_i(x) - \sum_{\bar{i}} f_{\bar{i}}(x)\,, \tag{14}$$

$$\Sigma(x) = \sum_i f_i(x) + \sum_{\bar{i}} f_{\bar{i}}(x)\,, \tag{15}$$

where the index $\bar{i}$ refers to antiquark flavors. The evolution equations then become

$$\frac{\mathrm{d}V^{(n)}}{\mathrm{d}t} = \frac{\alpha_{\mathrm{s}}}{2\pi}\, P_{\mathrm{qq}}^{(n)}\, V^{(n)}\,, \tag{16}$$

$$\frac{\mathrm{d}\Sigma^{(n)}}{\mathrm{d}t} = \frac{\alpha_{\mathrm{s}}}{2\pi}\left[P_{\mathrm{qq}}^{(n)}\,\Sigma^{(n)} + 2n_{\mathrm{f}}\, P_{\mathrm{qg}}^{(n)} f_{\mathrm{g}}^{(n)}\right], \tag{17}$$

$$\frac{\mathrm{d}f_{\mathrm{g}}^{(n)}}{\mathrm{d}t} = \frac{\alpha_{\mathrm{s}}}{2\pi}\left[P_{\mathrm{gq}}^{(n)}\,\Sigma^{(n)} + P_{\mathrm{gg}}^{(n)} f_{\mathrm{g}}^{(n)}\right]. \tag{18}$$

We note that the equation for the valence density decouples from the evolution of the gluon and singlet densities, which are coupled among themselves. This is physically very reasonable because the contribution to the quark and the antiquark densities coming from the evolution of gluons (via their splitting into $\mathrm{q\bar{q}}$ pairs) is the same in the perturbation theory, and it cancels in the definition of the valence. The valence therefore only evolves because of gluon emission. On the contrary, gluons and $\mathrm{q\bar{q}}$ pairs in the proton *sea* evolve into one another.

The first moment of $V(x)$, $V^{(1)} = \int_0^1 \mathrm{d}x\, V(x)$, counts the number of valence quarks. We therefore expect it to be independent of Q^2:

$$\frac{\mathrm{d}V^{(1)}}{\mathrm{d}t} \equiv 0 = \frac{\alpha_{\mathrm{s}}}{2\pi}\, P_{\mathrm{qq}}^{(1)}\, V^{(1)} = 0\,. \tag{19}$$

Because $V^{(1)}$ itself is different from 0, we obtain a constraint on the first moment of the splitting function: $P_{\mathrm{qq}}^{(1)} = 0$. This constraint is satisfied by including the effect of the virtual corrections, which generate a contribution to $P_{\mathrm{qq}}(z)$ proportional to $\delta(1-z)$. This correction is incorporated in $P_{\mathrm{qq}}(z)$ by reinterpreting it as a distribution,

$$P_{\mathrm{qq}}(z) \to \left(\frac{1+z^2}{1-z}\right)_+\,, \tag{20}$$

where the so-called $+$-distribution corresponding to a function $g(x)$ is defined by

$$\int_0^1 \left[g(x)\right]_+ f(x)\,\mathrm{d}x \equiv \int_0^1 g(x)\left[f(x) - f(1)\right]\mathrm{d}x\,. \tag{21}$$

By definition, $\int_0^1 \mathrm{d}z P_{\mathrm{qq}}(z) = 0$, and the valence sum rule is obeyed at all Q^2.

Another sum rule that is independent of Q^2 is the momentum sum rule, which imposes the constraint that all of the momentum of the proton is carried by its constituents (valence plus sea plus gluons):

$$\int_0^1 \mathrm{d}x\, x\left(\sum_{i,\bar{i}} f_i(x) + f_{\mathrm{g}}(x)\right) \equiv \Sigma^{(2)} + f_{\mathrm{g}}^{(2)} = 1\,. \tag{22}$$

Once more, this relation should hold for all Q^2 values, and it can be proved by using the evolution equations that this implies

$$P_{\mathrm{qq}}^{(2)} + P_{\mathrm{gq}}^{(2)} = 0\,, \tag{23}$$

$$P_{\mathrm{gg}}^{(2)} + 2n_{\mathrm{f}}\, P_{\mathrm{qg}}^{(2)} = 0\,. \tag{24}$$

Using the definition of the second moment and the explicit expressions of the P_{qq} and P_{gq} splitting functions, it can be verified that the first condition is satisfied automatically. The

[2] The expressions given here are strictly valid only for $x \neq 1$. The slight modifications required to extend them to $x = 1$ are justified and introduced in the next section.

second condition is satisfied by including the virtual effects in the gluon propagator, which contribute a term proportional to $\delta(1-x)$. It is a simple exercise to verify that the final form of the $P_{gg}(x)$ splitting function satisfying Eqn (24) is

$$P_{gg} \to 2C_A\left\{\frac{x}{(1-x)_+}+\frac{1-x}{x}+x(1-x)\right\} + \delta(1-x)\left[\frac{11C_A-2n_f}{6}\right]. \qquad (25)$$

2.3 Solution of the evolution equations

The evolution equations formulated in the previous section can be solved analytically in moment space. The boundary conditions are given by the moments of the parton densities at a given scale μ, where, in principle, they can be obtained from direct measurement. The solution at different values of the scale Q can then be obtained by numerically inverting the expression for the moments back to x space. The resulting evolved densities can then be used to calculate cross sections for an arbitrary process involving hadrons, at an arbitrary scale Q. We limit ourselves to studying some properties of the analytic solutions, and present and comment on some plots obtained from numerical studies available in the literature.

It is easy to show that the solution of the evolution equation for the valence density is given by

$$V^{(n)}(Q^2) = V^{(n)}(\mu^2)\left(\frac{\log Q^2/\Lambda^2}{\log \mu^2/\Lambda^2}\right)^{P_{qq}^{(n)}/2\pi b_0} = V^{(n)}(\mu^2)\left[\frac{\alpha_s(\mu^2)}{\alpha_s(Q^2)}\right]^{P_{qq}^{(n)}/2\pi b_0}, \qquad (26)$$

where the running of $\alpha_s(\mu^2)$ has to be taken into account to obtain the correct result. Because all moments $P^{(n)}$ are negative, the evolution to larger values of Q makes the valence distribution softer and softer. This is physically reasonable, since the only thing that the valence quarks can do is lose energy because of gluon emission.

The solutions for the gluon and singlet distributions f_g and Σ can be obtained by diagonalizing the 2×2 system in Eqns (17) and (18). We study the case of the second moments, which correspond to the momentum fractions carried by quarks and gluons separately. In the asymptotic limit, $\Sigma^{(2)}$ tends to a constant, and $\mathrm{d}\Sigma^{(2)}/\mathrm{d}t = 0$. Using the momentum sum rule, we then have

$$P_{qq}^{(2)}\,\Sigma^{(2)} + 2n_f\,P_{qg}^{(2)} f_g^{(2)} = 0\,, \qquad (27)$$

$$\Sigma^{(2)} + f_g^{(2)} = 1\,. \qquad (28)$$

The solution of this system is

$$\Sigma^{(2)} = \frac{1}{1+4C_F/n_f} \quad \left(=\frac{15}{31} \quad \text{for } n_f = 5\right), \qquad (29)$$

$$f_g^{(2)} = \frac{4C_F}{4C_F+n_f} \quad \left(=\frac{16}{31} \quad \text{for } n_f = 5\right). \qquad (30)$$

As a result, the fraction of momentum carried by gluons is asymptotically approximately 50% of the total proton momentum. It is interesting to note that the value of 50% is already measured experimentally at rather low values of Q. The first deep-inelastic ep experiments that exposed the possible presence of quarks in the proton revealed in fact that only approximately 50% of the proton momentum is carried by charged constituents. This was one of the early pieces of evidence for the existence of gluons. The near coincidence of the low-energy value with the asymptotic one is nevertheless rather accidental, and results from a partial cancellation between the Q^2 evolution and the increasing value of n_f as the heavy-flavor thresholds are being crossed.

2.4 Example: quantitative evolution of parton densities

As mentioned above, a complete solution for the evolved parton densities in the x space can only be obtained numerically. This has been done by several groups (see [15, 16] for a review), and the results are continuously being updated [17–21] by including the most up-to-date experimental results used for the determination of the input densities at a fixed scale. The left-land side of Fig. 7a shows the up-quark valence momentum density at various Q scales, as obtained from one of these studies. We note the softening at larger scales and the clear $\log Q^2$ evolution. As Q^2 increases, the valence quarks emit more and more radiation, since they change direction over a shorter amount of time (larger acceleration). They therefore lose more momentum to the emitted gluons, and their spectrum becomes softer. The most likely momentum fraction carried by a valence up-quark in the proton ranges from $x \sim 20\%$ at $Q = 3$ GeV to $x \lesssim 10\%$ at $Q = 1000$ GeV. We also note that the density vanishes at small x.

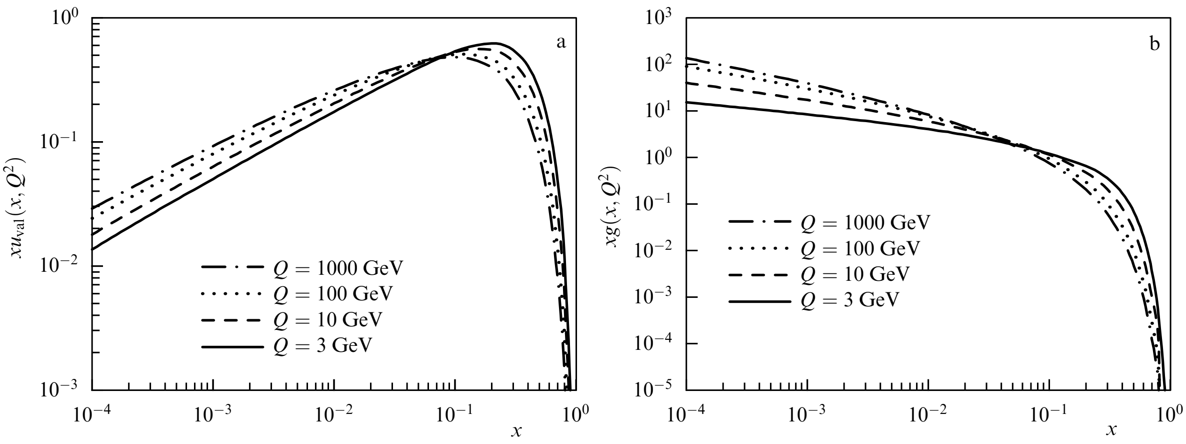

Figure 7. (a) Valence up-quark momentum density distribution for different scales Q. (b) Gluon momentum density distribution.

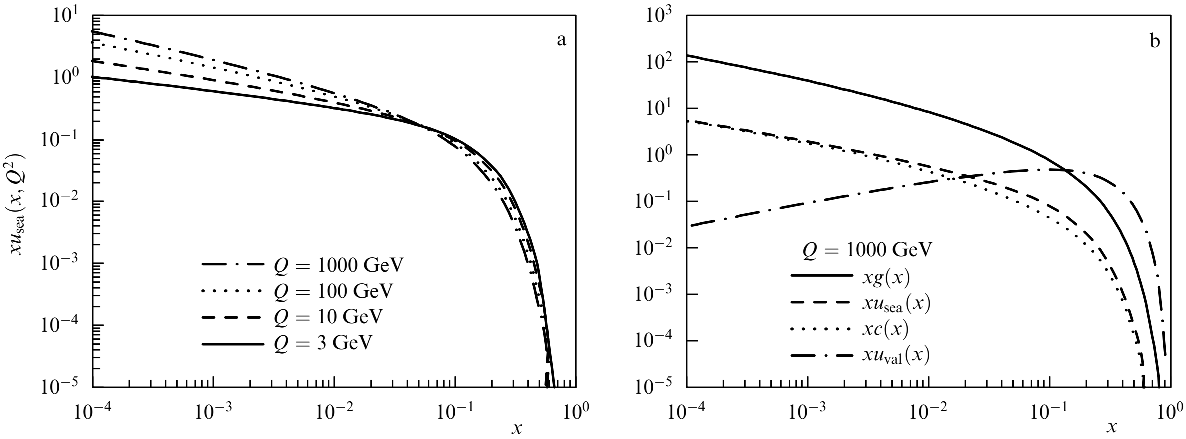

Figure 8. (a) Sea up-quark momentum density distribution for different scales Q. (b) Momentum density distribution for several parton species at $Q = 1000$ GeV.

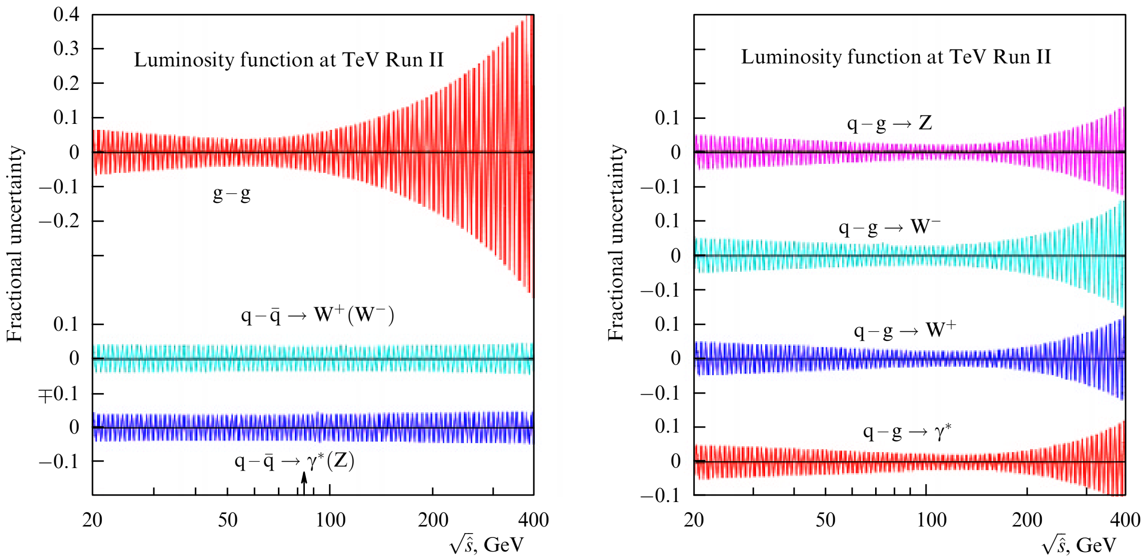

Figure 9. Uncertainty in the parton luminosity functions at the Tevatron [22].

The right-hand side of Fig. 7b shows the gluon momentum density. It increases at small x, with an approximate $g(x) \sim 1/x^{1+\delta}$ behavior and $\delta > 0$ slowly increasing at large Q^2. This low-x increase is due to the $1/x$ emission probability for the radiation of gluons, which was discussed in the previous section and which is represented by the $1/x$ factors in the $P_{\rm gq}(x)$ and $P_{\rm gg}(x)$ splitting functions. As Q^2 increases, we find an increasing number of gluons at small x as a result of the increased radiation of quarks, as well as of the harder gluons.

The left-hand side of Fig. 8a shows the evolution of the up-quark sea momentum density. The shape and evolution match those of the gluon density, a consequence of the fact that sea quarks come from the splitting of gluons. Since the gluon splitting probability is proportional to $\alpha_{\rm s}$, the approximate ratio sea/gluon ~ 0.1, which can be obtained by comparing Figs 7 and 8, is perfectly justified.

Finally, the momentum densities for gluons, up-sea, charm, and up-valence distributions are shown, for $Q = 1000$ GeV, in the right-hand side of Fig. 8b. We note that $\rm u_{sea}$ and charm are approximately the same at very large Q and small x, which we discuss in more detail in the next subsection. The proton momentum is mostly carried by valence quarks and gluons. The contribution of sea quarks is negligible.

Parton densities are extracted from experimental data. Their determination is therefore subject to the statistical and systematic uncertainties of the experiments and of the theoretical analysis (e.g., the treatment of nonperturbative effects and the impact of missing higher-order perturbative corrections). Techniques have been introduced recently to take these uncertainties into account and to evaluate their impact on concrete observables. A summary of such an analysis [22] is given in Figs 9 (for the Tevatron) and 10 (for the LHC). The uncertainty bands for partonic luminosities [3] corresponding to various initial-state channels, such as gg, qg, or q$\bar{\rm q}$, are plotted The partonic flux is given as a function of the partonic CM invariant mass $\hat{s}$. Obvious features include the increase in the uncertainty of the gg density at large mass, corresponding to the lack of data covering the large-x region of the gluon density. As a result, we note for example that the uncertainty in the gg $\to$ t$\bar{\rm t}$ production rate at the LHC is

[3] For the definition of parton luminosity, see Section 4.1.

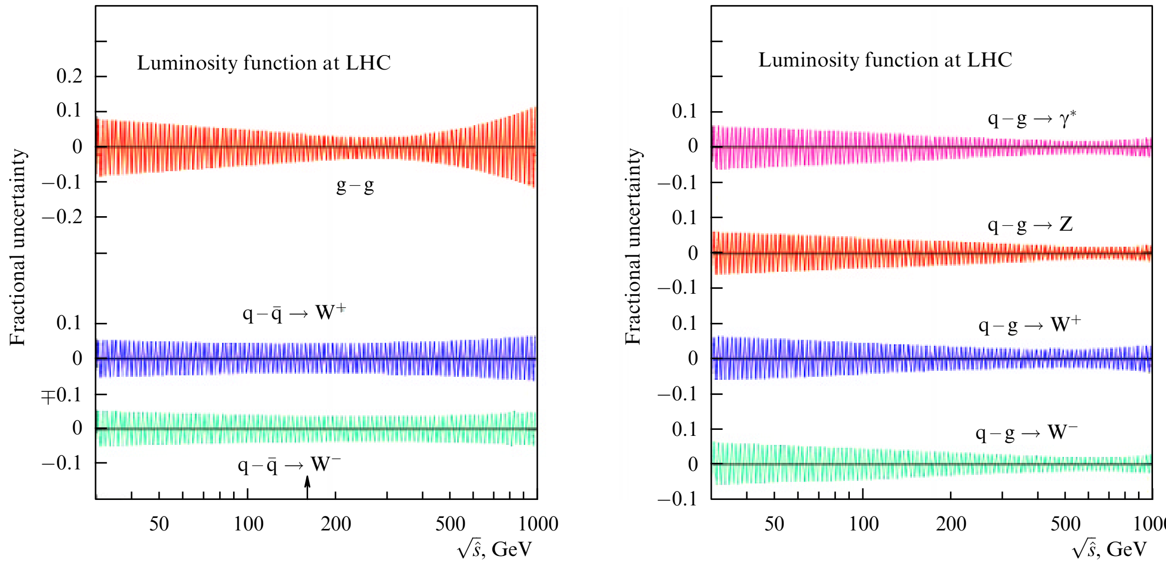

Figure 10. Uncertainty in the parton luminosity functions at the LHC [22].

smaller than at the Tevatron, since the relative range of mass (just above $2m_t \sim 350$ GeV) corresponds at the LHC to gluon densities in better-explored regions of x.

2.5 Example: the charm content of the proton

If the virtuality of the external probe is large enough, the time scale of the hard interaction is so short that gluon fluctuations into virtual heavy quark states can be directly exposed, and the virtual heavy quarks (charm quarks in our example) can be brought on shell via the interaction with the photon (see Fig. 11). To the external photon, it therefore appears as if the proton contained some charm. In the case of the gluons and of light quarks, the boundary condition for the DGLAP evolution at small Q is nonperturbative and cannot be derived from first principles, but in the case of a heavy quark Q, the boundary condition $f_Q(x, Q_0) = 0$ holds at a scale $Q_0 \sim m_Q$ that is large enough for the perturbation theory to apply. The charm density can be calculated assuming that the heavy-quark density itself is 0 at $Q \sim m_c$, and builds up according to the DGLAP evolution equation

$$\frac{\mathrm{d}c(x,Q)}{\mathrm{d}t} = \frac{\alpha_s}{2\pi} \int_x^1 \frac{\mathrm{d}y}{y}\, g(y,Q)\, P_{qg}\left(\frac{x}{y}\right). \qquad (31)$$

Assuming that the gluon density behaves as $g(x,Q) \sim A/x$, which is a first approximation to a bremsstrahlung spectrum,

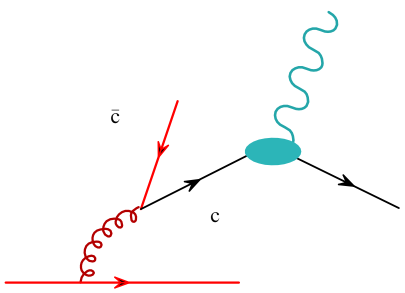

Figure 11. Gluon evolution leading to a charm quark content of the proton.

we can easily calculate

$$\frac{\mathrm{d}c(x,Q)}{\mathrm{d}t} = \frac{\alpha_s}{2\pi} \int_x^1 \frac{\mathrm{d}y}{y}\, g\left(\frac{x}{y}, Q\right) P_{qg}(y)$$
$$= \frac{\alpha_s}{2\pi} \int_x^1 \mathrm{d}y\, \frac{A}{x}\,\frac{1}{2}\left[y^2 + (1-y)^2\right] = \frac{\alpha_s}{6\pi}\,\frac{A}{x}\,, \qquad (32)$$

$$c(x,Q) \sim \frac{\alpha_s}{6\pi} \log\left(\frac{Q^2}{m_c^2}\right) g(x,Q)\,. \qquad (33)$$

The charm density is therefore proportional to the gluon density, up to an overall factor proportional to α_s. As Q becomes very large, the effect of the quark mass becomes subleading, and we expect all sea quarks to reach asymptotically the same density.

Although this is a simplified approach to the estimate of the heavy-quark density of the proton, the approximation is rather good. This is shown by the plots in Fig. 12, which compare the charm and bottom PDF given by Eqn (33) with the result extracted from a full set of PDFs. The solid histograms in these plots represent the exact result for three values of the evolution scale Q. The diamonds give the approximate results. The agreement is very good at small x and at the smaller values of Q. At larger x, the approximation deteriorates because the assumption that $g(x) \sim 1/x$ is no longer valid in that case. At higher scales Q, the exact result becomes smaller than the approximate one, since the latter neglects the momentum loss due to the higher-order gluon radiation (namely, the contributions to the evolution equation proportional to $P_{qq}(y)\, Q(x/y)$). Of course, any accurate calculation of cross sections involving initial-state heavy quarks must use exact results, but it is interesting to see that even in such a complex process, it is possible to identify useful analytic approximations that yield good order-of-magnitude estimates!

3. The final-state evolution of quarks and gluons

In the preceding section, we discussed the initial-state evolution of quarks and gluons as the proton approaches a hard collision. We study here how quarks and gluons evolve

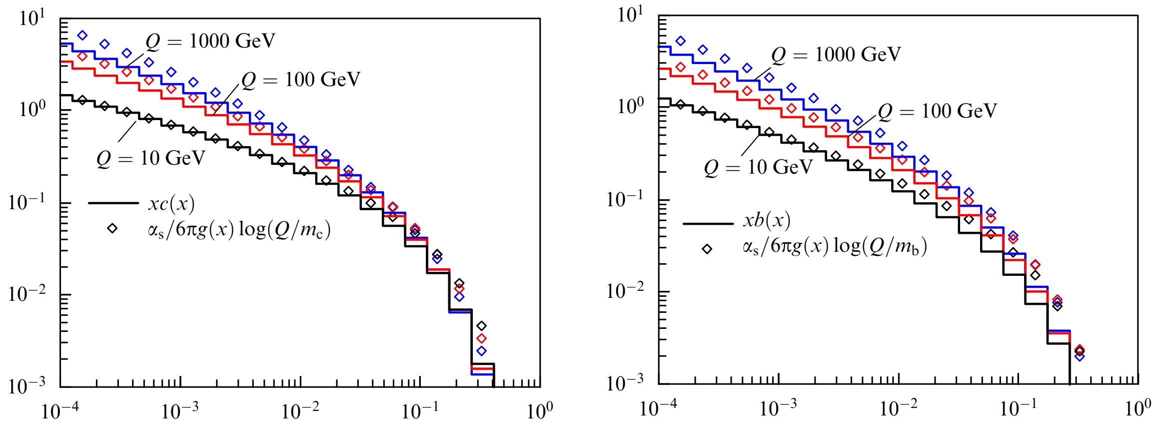

Figure 12. Charm and bottom quark PDFs obtained from the exact and approximate evolutions.

after emerging from the hard process and finally transform into hadrons, neutralizing their colors. We start by considering the simplest case of e^+e^- collisions, which provide the cleanest environment in which to study applications of QCD at high energy. This is where theoretical calculations have today reached their best accuracy and where experimental data are the most precise, especially thanks to the huge number of statistics accumulated by LEP, LEP2, and SLC. The key process is the annihilation of the e^+e^- pair into a virtual photon or Z^0 boson, which subsequently decay to a $q\bar{q}$ pair. e^+e^- collisions therefore have the big advantage of providing an almost point-like source of quark pairs, and hence, in contrast to the case of interactions involving hadrons in the initial state, at least the state of the quarks at the beginning of the interaction process is known very precisely.

Nevertheless, it is by no means obvious that this information is sufficient to predict the properties of the hadronic final state. We know that this final state is clearly not simply a $q\bar{q}$ pair but some high-multiplicity set of hadrons. For example, as shown in Fig. 13, the average multiplicity of charged hadrons in the decay of a Z^0 boson is approximately 20. It is therefore not obvious that a calculation done using the simple picture $e^+e^- \to q\bar{q}$ (see Fig. 14) has anything to do with reality. For example, it is not clear why we do not need to calculate $\sigma(e^+e^- \to q\bar{q}g\ldots g\ldots)$ for all possible gluon multiplicities to obtain an accurate estimate of $\sigma(e^+e^- \to \text{hadrons})$. And since in any case the final state is not made up of q's and g's, but of π's, K's, ρ's, etc., why would $\sigma(e^+e^- \to q\bar{q}g\ldots g)$ be enough?

The solution to this puzzle lies both in the question of time and energy scales, and in the dynamics of QCD. When a $q\bar{q}$ pair is produced, the force binding q and $\bar{q}$ is proportional to $\alpha_s(s)$ ($\sqrt{s}$ being the e^+e^- center-of-mass energy). Therefore, it is weak, and q and $\bar{q}$ behave to good approximation like free particles. The radiation emitted in the first instants after the pair creation is also perturbative, and it stays so until a time after creation of the order of $(1\ \text{GeV})^{-1}$, when radiation with wavelengths $\gtrsim (1\ \text{GeV})^{-1}$ starts being emitted. At this scale, the coupling constant is large, and nonperturbative phenomena and hadronization start playing a role. However, as we show in what follows, color emission during the perturbative evolution organizes itself in such a way as to form color-neutral, low-mass, parton clusters highly localized in phase space. As a result, the complete color neutralization (i.e., the hadronization) does not involve long-range interactions between partons far away in phase space. This is very important, because the forces acting among colored objects at this time scale would be huge. If the perturbative evolution were to separate color-singlet $q\bar{q}$ pairs far apart, the final-state interactions occurring during the hadronization phase would totally upset the structure of the final state.

In this picture, the identification of the perturbative cross section $\sigma(e^+e^- \to q\bar{q})$ with observable, high-multiplicity hadronic final states is realized by jets, namely, by collimated streams of hadrons that are the final result of the perturbative and nonperturbative evolution of each quark.

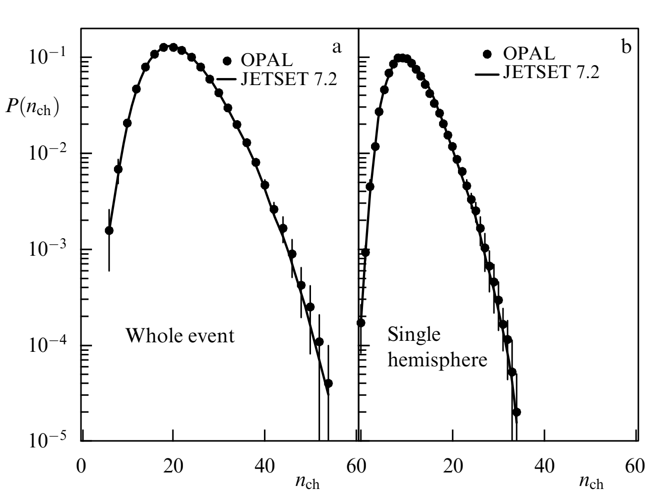

Figure 13. Charged particle multiplicity distribution in Z^0 decays.

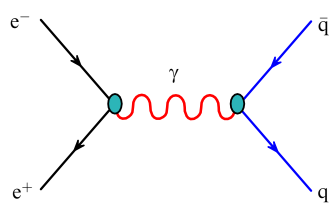

Figure 14. Tree-level production of a $q\bar{q}$ pair in e^+e^- collisions.

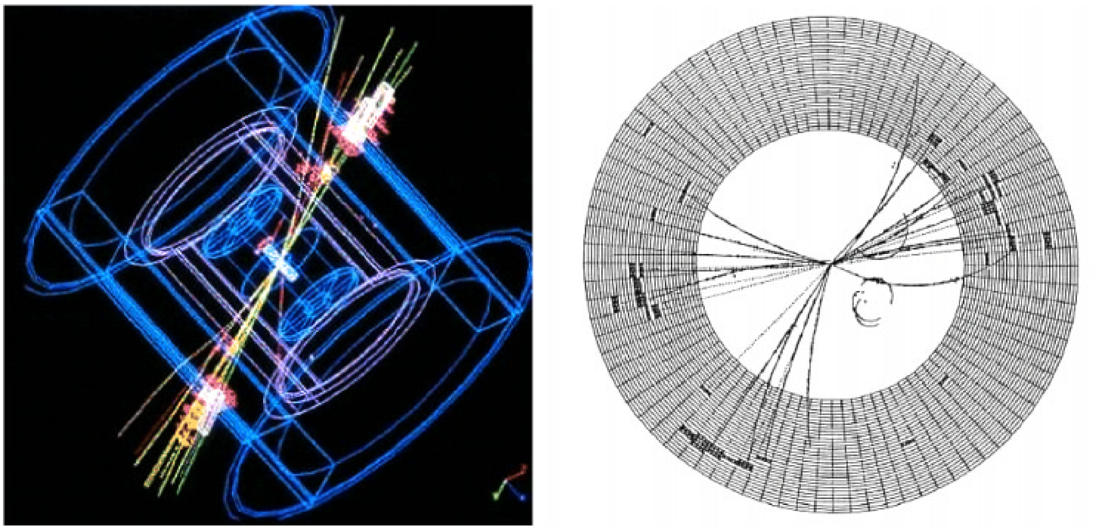

Figure 15. Experimental pictures of 2- and 3-jet final states from e^+e^- collisions.

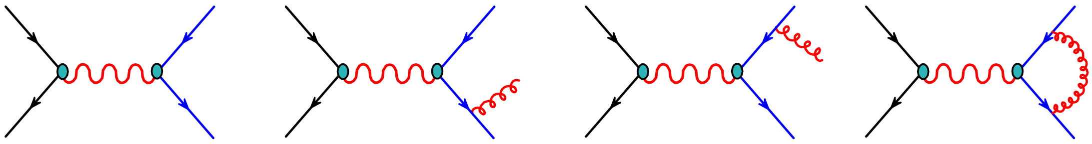

Figure 16. $O(\alpha_s)$ corrections to the tree-level $e^+e^- \to q\bar{q}$ process.

The large multiplicity of the final states, shown in Fig. 13, corresponds to the many particles that emerge from the collinear emissions of many gluons from each quark. The dynamics of these emissions lead these particles to primarily follow the direction of the primary quark, and the emergent bundle, the jet, inherits the kinematics of the initial quark. This is shown in the left image of Fig. 15. Three-jet events, shown in the right image of Fig. 15, arise from $O(\alpha_s)$ corrections to the tree-level process, specifically, to diagrams such as those shown in Fig. 16.

An important additional result of this 'preconfining' evolution is that the memory of where the local color-neutral clusters came from is totally lost, and we therefore expect the properties of hadronization to be universal: a model that describes hadronization at a given energy should work equally well at some other energy. Furthermore, so much time has passed since the original $q\bar{q}$ creation that the hadronization phase cannot significantly affect the total hadron production rate. Perturbative corrections due to the emission of the first hard partons should be calculable in the perturbation theory, providing a finite, meaningful cross section.

The nature of nonperturbative corrections to this picture can be explored. For example, it can be proved that the leading correction to the total rate $R_{e^+e^-}$ is of the order of F/s^2, where $F \propto \langle 0|\alpha_s F^a_{\mu\nu} F^{\mu\nu a}|0\rangle$ is the so-called gluon condensate. Because $F \sim O\,(1\ \mathrm{GeV}^4)$, these nonperturbative corrections are usually very small. For example, they are $O(10^{-8})$ at the Z^0 peak. Corrections scaling as Λ^2/s or $\Lambda/\sqrt{s}$ can nevertheless appear in other less inclusive quantities, such as event shapes or fragmentation functions.

We now return to the perturbative evolution and devote the first part of this section to justifying the picture given above.

3.1 Soft gluon emission

Emission of soft gluons plays a fundamental role in the evolution of the final state [6, 9]. Soft gluons are emitted with a large probability because the emission spectrum behaves as $\mathrm{d}E/E$, typical of bremsstrahlung familiar in QED. They provide the seed for the bulk of the final-state multiplicity of hadrons. The study of soft-gluon emission is made easier by the simplicity of their couplings. Being soft (i.e., long wavelength), they are insensitive to the details of the very-short-distance dynamics: they cannot distinguish features of the interactions that occur on time scales shorter than their wavelength. They are also insensitive to the spin of the partons: the only feature they are sensitive to is the color charge. To prove this, we consider soft-gluon emission in the $q\bar{q}$ decay of an off-shell photon:

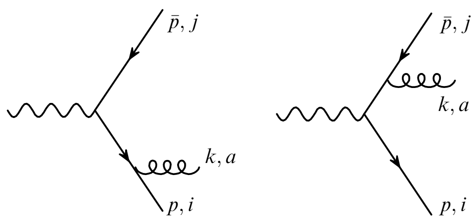

$$
\begin{aligned}
A_{\mathrm{soft}} &= \bar{u}(p)\,\epsilon(k)\,(\mathrm{i}g)\,\frac{-\mathrm{i}}{\not{p}+\not{k}}\,\Gamma^{\mu}\,v(\bar{p})\;\lambda^a_{ij} \\
&\quad + \bar{u}(p)\,\Gamma^{\mu}\,\frac{\mathrm{i}}{\not{\bar{p}}+\not{k}}\,(\mathrm{i}g)\,\epsilon(k)\,v(\bar{p})\,\lambda^a_{ij} \\
&= \left[\frac{g}{2pk}\,\bar{u}(p)\,\epsilon(k)\,(\not{p}+\not{k})\,\Gamma^{\mu}\,v(\bar{p}) \right.\\
&\quad \left. -\frac{g}{2\bar{p}k}\,\bar{u}(p)\,\Gamma^{\mu}\,(\not{\bar{p}}+\not{k})\,\epsilon(k)\,v(\bar{p})\right]\lambda^a_{ij}\,. \qquad (34)
\end{aligned}
$$

The generic symbol Γ_μ is used to describe the interaction vertex with the photon to stress that the subsequent manipulations are independent of the specific form of Γ_μ. In particular, Γ_μ can represent an arbitrarily complicated vertex form factor. Neglecting the factors $\not{k}$ in the numerators (because $k \ll p, \bar{p}$ by the definition of being soft) and using the Dirac equations, we obtain

$$A_{\text{soft}} = g\lambda^a_{ij}\left(\frac{p\epsilon}{pk} - \frac{\bar{p}\epsilon}{\bar{p}k}\right) A_{\text{Born}} \,. \tag{35}$$

We then conclude that soft-gluon emission amplitude is given by an emission factor times the Born-level amplitude. From this exercise, we can extract general Feynman rules for soft-gluon emission:

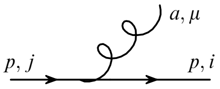

$$= g\lambda^a_{ij} 2p^\mu \,. \tag{36}$$

An analogous exercise leads to $g \to gg$ soft-emission rules

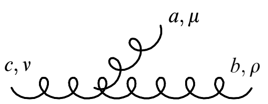

$$= \mathrm{i}gf^{abc} 2p^\mu g^{\nu\rho} \,. \tag{37}$$

We now consider the 'decay' of a virtual gluon into a quark pair: One more diagram should be added to those considered in the case of the electroweak decay. The fact that the quark pair is no longer in a color-singlet state makes things a bit more interesting:

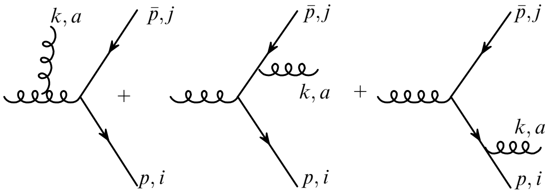

$$\begin{aligned}
&\overset{k\to 0}{=}\left[\mathrm{i}gf^{abc}\lambda^c_{ij}\left(\frac{Q\epsilon}{Qk}\right) + g(\lambda^b\lambda^a)_{ij}\left(\frac{p\epsilon}{pk}\right)\right.\\
&\quad\left. - g(\lambda^a\lambda^b)_{ij}\left(\frac{\bar{p}\epsilon}{\bar{p}k}\right)\right] A_{\text{Born}}\\
&\quad = g(\lambda^a\lambda^b)_{ij}\left[\frac{Q\epsilon}{Qk} - \frac{\bar{p}\epsilon}{\bar{p}k}\right] + g(\lambda^b\lambda^a)_{ij}\left[\frac{p\epsilon}{pk} - \frac{Q\epsilon}{Qk}\right].
\end{aligned}\tag{38}$$

The two factors correspond to the two possible ways color can flow in this process:

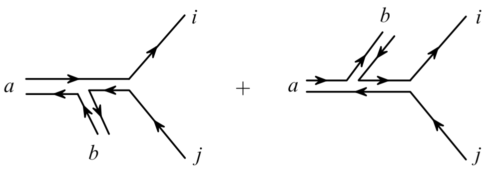

(39)

The basis for this representation of the color flow is the following diagram, which makes the relation between the colors of the quark, antiquark, and gluon entering a QCD vertex explicit:

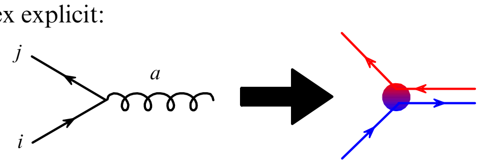

(40)

We can therefore represent the gluon with a double line, one line carrying the color inherited from the quark, the other carrying the anticolor inherited from the antiquark. In the first diagram in (39), the antiquark (color label j) is color-connected to the soft gluon (color label b), and the quark (color label i) is connected to the decaying gluon (color label a). In the second case, the order is reversed. The two emission factors correspond to the emission of the soft gluon from the antiquark and from the quark line. After the total amplitude is squared and summed over initial-state and final-state colors, the interference between the two pieces is suppressed by $1/N^2$ relative to the individual squares:

$$\begin{aligned}
\sum_{a,b,i,j} \left|(\lambda^a\lambda^b)_{ij}\right|^2 &= \sum_{a,b} \mathrm{tr}(\lambda^a\lambda^b\lambda^b\lambda^a)\\
&= \frac{N^2-1}{2} C_{\mathrm{F}} = O(N^3)\,,
\end{aligned}\tag{41}$$

$$\begin{aligned}
\sum_{a,b,i,j} (\lambda^a\lambda^b)_{ij}[(\lambda^b\lambda^a)_{ij}]^* &= \sum_{a,b} \mathrm{tr}(\lambda^a\lambda^b\lambda^a\lambda^b)\\
&= \frac{N^2-1}{2}\underbrace{\left(C_{\mathrm{F}} - \frac{C_{\mathrm{A}}}{2}\right)}_{-1/(2N)} = O(N)\,.
\end{aligned}\tag{42}$$

As a result, the emission of a soft gluon can be described, to the leading order in $1/N^2$, as the incoherent sum of the emission from the two color currents. The ability to separate these emissions as incoherent sums is the basic fact that allows a sequential, Markovian description of the parton-shower evolution as implemented in numerical simulations of the hadronic final state of hard collisions. The neglect of subleading $1/N^2$ contributions is therefore an intrinsic approximation of all such approaches.

3.2 Angular ordering for soft-gluon emission

The results presented above have important consequences for the perturbative evolution of quarks. A key property of soft-gluon emission is the so-called *angular ordering* (for an overview of color coherence and its relation to angular ordering, see [9, 23]). This phenomenon consists in the continuous reduction of the opening angle at which successive soft gluons are emitted by the evolving quark. As a result, this radiation is confined within smaller and smaller cones around the quark direction, and the final state looks like a collimated jet of partons. In addition, the structure of the color flow during the jet evolution forces the $q\bar{q}$ pairs that are in a color-singlet state to be close in phase space, thereby achieving the preconfinement of color-singlet clusters alluded to at the beginning of this section.

We start by proving the property of color ordering. We consider the $q\bar{q}$ pair produced by the decay of a rapidly moving virtual photon. The amplitude for the emission of a soft gluon was given in Eqn (35). Squaring, summing over colors, and including the gluon phase space, we obtain the result

$$\begin{aligned}
\mathrm{d}\sigma_g &= \sum |A_{\text{soft}}|^2 \frac{\mathrm{d}^3k}{(2\pi)^3 2k^0} = \sum |A_0|^2 \frac{-2p^\mu\bar{p}^\nu}{(pk)(\bar{p}k)}\, g^2\\
&\times \sum \epsilon_\mu\epsilon^*_\nu \frac{\mathrm{d}^3k}{(2\pi)^3 2k^0}\\
&= \mathrm{d}\sigma_0 \frac{2(p\bar{p})}{(pk)(\bar{p}k)}\, g^2 C_{\mathrm{F}}\left(\frac{\mathrm{d}\phi}{2\pi}\right)\frac{k^0\,\mathrm{d}k^0}{8\pi^2}\,\mathrm{d}\cos\theta\\
&= \mathrm{d}\sigma_0 \frac{\alpha_{\mathrm{s}} C_{\mathrm{F}}}{\pi}\frac{\mathrm{d}k^0}{k^0}\frac{\mathrm{d}\phi}{2\pi}\frac{1-\cos\theta_{ij}}{(1-\cos\theta_i)(1-\cos\theta_{jk})}\,\mathrm{d}\cos\theta\,,
\end{aligned}\tag{43}$$

where $\theta_{\alpha\beta} = \theta_\alpha - \theta_\beta$, and i, j, and k respectively refer to the q, $\bar{\mathrm{q}}$, and gluon directions. We can write the identity

$$\frac{1-\cos\theta_{ij}}{(1-\cos\theta_{ik})(1-\cos\theta_{jk})} = \frac{1}{2}\left(\frac{\cos\theta_{jk}-\cos\theta_{ij}}{(1-\cos\theta_{ik})(1-\cos\theta_{jk})} + \frac{1}{1-\cos\theta_{ik}}\right) + \frac{1}{2}[i \leftrightarrow j] \equiv W_{(i)} + W_{(j)} \,. \tag{44}$$

We would like to interpret the two functions $W_{(i)}$ and $W_{(j)}$ as the probabilities of radiation from the quark and antiquark lines. Each of them is in fact only singular in the limit of gluon emission parallel to the respective quark:

$$W_{(i)} \text{ finite if } k \parallel j \; (\cos\theta_{jk} \to 1)\,, \tag{45}$$

$$W_{(j)} \text{ finite if } k \parallel i \; (\cos\theta_{ik} \to 1)\,. \tag{46}$$

But the interpretation as probabilities is limited by the fact that neither $W_{(i)}$ nor $W_{(j)}$ are positive definite. However, it can easily be proved that

$$\int \frac{\mathrm{d}\phi}{2\pi}\, W_{(i)} = \begin{cases} \dfrac{1}{1-\cos\theta_{ik}} & \text{at } \theta_{ik} < \theta_{ij}\,, \\ 0 & \text{at } \theta_{ik} \geqslant \theta_{ij}\,, \end{cases} \tag{47}$$

where the integral gives the azimuthal average around the q direction. A similar result holds for $W_{(j)}$:

$$\int \frac{\mathrm{d}\phi}{2\pi}\, W_{(j)} = \begin{cases} \dfrac{1}{1-\cos\theta_{jk}} & \text{at } \theta_{jk} < \theta_{ij}\,, \\ 0 & \text{at } \theta_{jk} \geqslant \theta_{ij}\,. \end{cases} \tag{48}$$

As a result, the emission of soft gluons outside the two cones obtained by rotating the antiquark direction around the quark direction, and vice versa, averages to 0. Inside the two cones, we can consider the radiation from the emitters as being uncorrelated. In other words, the two color lines defined by the quark and antiquark currents act as independent emitters, and the quantum coherence (the effects of interference between the two graphs contributing to the gluon-emission amplitude) is accounted for by constraining the emission to take place within those fixed cones.

A simple derivation of angular ordering, which exhibits its physical origin more directly, can be obtained as follows. We consider Fig. 17a, which shows a Feynman diagram for the emission of a gluon from a quark line. The quark momentum is denoted by l and the gluon momentum by k, θ is the opening angle between the quark and the antiquark, and α is the angle between the nearest quark and the emitted gluon. We work in the double-log enhanced soft ($k^0 \ll l^0$) and collinear ($\alpha \ll 1$) regions. The internal quark propagator $p = l + k$ is off shell, setting the time scale for the gluon emission:

$$\Delta t \simeq \frac{1}{\Delta E} = \frac{l^0}{(k+l)^2} \;\to\; \Delta t \simeq \frac{1}{k^0\alpha^2}\,. \tag{49}$$

To resolve the quarks, the transverse wavelength of the gluon $\lambda_\perp = 1/E_\perp$ must be smaller than the separation between the quarks $b(t) \simeq \theta\,\Delta t$, giving the constraint $1/(\alpha k^0) < \theta\,\Delta t$. Using Eqn (49) for Δt, we arrive at the angular ordering constraint $\alpha < \theta$. Gluon emissions at an angle smaller than θ can resolve the two individual color quarks and are allowed;

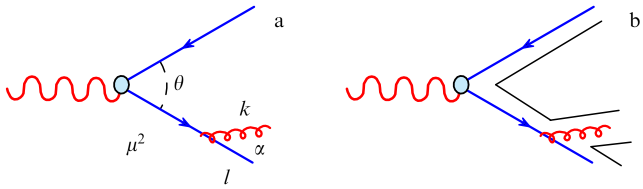

Figure 17. Radiation off the $\mathrm{q}\bar{\mathrm{q}}$ pair produced by an off-shell photon.

emissions at greater angles do not see the color charge and are therefore suppressed. In processes involving more partons, the angle θ is defined not by the nearest parton but by a color-connected parton (e.g., the parton that forms a color singlet with the emitting parton). Figure 17b shows the color connections for the $\mathrm{q}\bar{\mathrm{q}}$ event after the gluon is emitted. Color lines begin on quarks and end on antiquarks. Because gluons are color octets, they contain the beginning of one line and the end of another, as we showed in (39).

Repeating the exercise for emission of one additional gluon yields the same angular constraint, but applied to the color lines defined by the previously established *antenna*. As shown in Section 3.1, the $\mathrm{q}\bar{\mathrm{q}}\mathrm{g}$ state can be decomposed at the leading order in $1/N$ into two independent emitters, one given by the color line flowing from the gluon to the quark and the other given by the color line flowing from the antiquark to the gluon. The emission of the additional gluon must therefore be constrained to occur either within the cone formed by the quark and the gluon or within the cone formed by the gluon and the antiquark. In either case, the emission angle is smaller than the angle of the first gluon emission. This leads to the concept of angular ordering, with successive emission of soft gluons occurring within cones that become smaller and smaller, as in Fig. 18.

The fact that color always flows directly from the emitting parton to the emitted one, the collimation of the jet, and the softening of the radiation emitted at later stages ensure that partons forming a color-singlet cluster are close in phase space. As a result, hadronization (the nonperturbative process that binds color-singlet parton pairs together) occurs locally inside the jet and is not a long-distance phenomenon connecting partons far away in the evolution tree: only pairs of nearby partons are involved. In particular, there is no direct link between the precise nature of the hard process and the hadronization. These two phases are totally decoupled and, as in the case of partonic densities, we can infer that

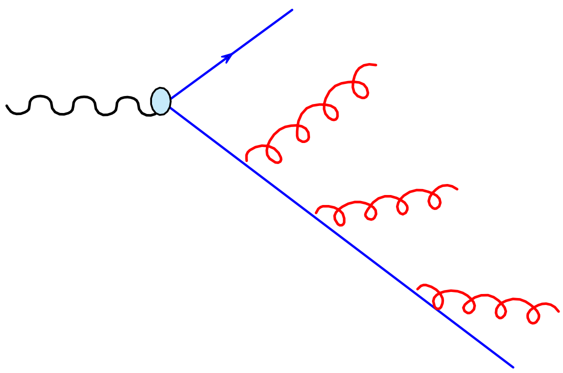

Figure 18. Collimation of soft gluon emission during the jet evolution.

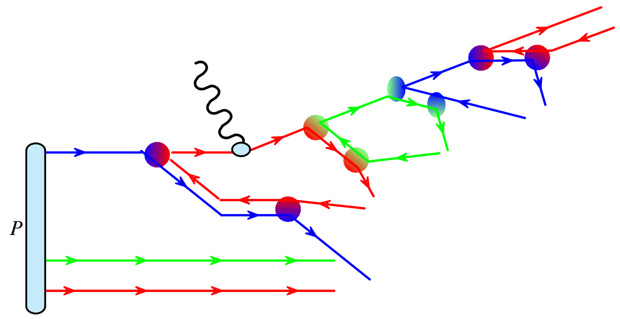

Figure 19. The color flow diagram for a deep inelastic scattering event.

hadronization factors from the hard process and can be described in a universal (i.e., hard-process independent) fashion. The inclusive properties of jets (e.g., the particle multiplicity, jet mass, and jet broadening) are independent of the hadronization model, up to corrections of the order of $(\Lambda/\sqrt{s})^n$ (for some integer power n, which depends on what is under observation), with $\Lambda \lesssim 1$ GeV.

The final picture, in the case of a deep inelastic scattering event, appears therefore as in Fig. 19. After being deflected by the photon, the struck quark emits the first gluon that takes away the quark color and passes on its own anticolor to the escaping quark. This gluon is therefore color-connected with the last gluon emitted before the hard interaction. As the final-state quark continues its evolution, more and more gluons are emitted, each time leaving their color behind and transmitting their anticolor to the emerging quark.

Angular ordering forces all these gluons to be close in phase space, until the evolution is stopped when the virtuality of the quark becomes of the order of the strong-interaction scale. The color of the quark is left behind, and when hadronization takes over, only the nearby color-connected gluons are transformed, with a phenomenological model, in hadrons. This mechanism for the transfer of color across subsequent gluon emissions is similar to what happens when a charge is placed near the surface of a dielectric medium. The medium becomes polarized, and a charge appears on its opposite end as a result of a sequence of local charge shifts, whereby neighboring atoms are polarized, as in Fig. 20.

We note that the transfer of color between the final-state jet and the jet associated with the initial state leads to the existence of one color-singlet cluster containing partons from both jets. Therefore, the particles arising from this cluster cannot be associated with either jet; they are hadrons whose source is a combination of two of the hard partons in the event. This feature is present in any hard process: it is an unavoidable consequence of the neutralization of the color of the partons involved in the hard scattering.

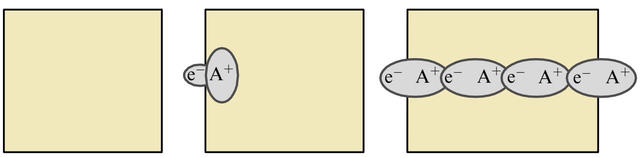

Figure 20. Charge transfer in a dieletric medium via a sequence of local polarizations.

3.3 Hadronization

Application of the perturbation theory to the evolution of a jet with the sequential emission of partons, governed by QCD splitting probabilities and angular ordering to enforce quantum mechanical quantum coherence, becomes invalid when the scale of the emissions reaches values in the range of 1 GeV. This is called the *infrared cutoff*. There are two reasons why we need to stop the emission of gluons at this scale. First, the perturbation theory does not allow controlling the domain below this scale, where the strong-coupling constant α_s becomes very large. Furthermore, we know that the number of physical particles that can be produced inside a jet must be finite, since the lightest object we can produce is a pion, and energy conservation sets a limit on how many pions can be created. This is different from what happens in a QED cascade, where the evolution of an accelerated charge can lead to the emission of an arbitrary number of photons. This is possible because the photon is massless and can have arbitrarily small energy. The gluons of a QCD cascade, on the contrary, must have sufficient energy to create pions.

When the perturbative evolution of the jet terminates, we are left with some number of gluons. As shown in Section 3.1 and displayed in Fig. 19, these gluons are pairwise color connected. As two color-connected gluons travel away from each other, a constant force pulls them together. Phenomenological models (see Ref. [6] for a more complete review) are then used to describe how this force determines the evolution of the system from this point on. We here describe the so-called *cluster model* [24], implemented in the HERWIG Monte Carlo generator [25, 26], but the main qualitative features are shared by other alternatives, such as the Lund string approach [27] implemented in the PYTHIA generator [28, 29].

Most of the hadrons emerging from the evolution of a jet are known to be made of quarks; glueballs, i.e., hadrons made of bound gluons, are expected to exist, but their production is greatly suppressed compared to that of quark-made particles. For this reason, the first step in the description of hadronization is to assume that the force among gluons rips them apart into a $q\bar{q}$ pair, and that these quarks act as seeds for hadron production. The break-up into quarks is not parameterized using the DGLAP $g \to q\bar{q}$ splitting function because we are dealing here with a nonperturbative transition. Therefore, a pure phase-space 'decay' of the gluon into the $q\bar{q}$ pair is typically used, with the relative probabilities of selecting the various active flavors (up, down, strange, etc.) introduced as phenomenological parameters. The quark q_i from one gluon (i representing the flavor) then forms a color-singlet pair with the antiquark $\bar{q}_j$ emerging from the break-up of the neighboring gluon. But this color-singlet $q_i\bar{q}_j$ pair cannot directly form a hadron, since in general the quarks are still moving apart, and the invariant mass of the pair would not coincide with the mass of an existing physical state.

As the quarks separate under a constant force, however, their kinetic energy turns into a linearly increasing potential energy. The potential energy accumulated in the system can be converted into a new quark–antiquark pair, $q_k\bar{q}_k$, once its value exceeds the relevant mass threshold. We are now left with two color-singlet pairs, $q_i\bar{q}_k$ and $q_k\bar{q}_j$. When converting the potential energy into the mass and kinetic energy of the newly produced pair, we can use the freedom in selecting the spatial kinematics of q_k and $\bar{q}_k$ such that both $q_i\bar{q}_k$ and $q_k\bar{q}_j$ invariant masses coincide with some resonance with the proper flavor. The residual energy of the system is then assumed to be entirely kinetic, and the two resonances fly away freely. Once again, phenomenological parameters can be associated with the probabilities of selecting flavors k of a given type. Since the pair of flavor indices ik does not specify a hadron uniquely (e.g., a $\mathrm{u\bar{d}}$ system could by a π^+, a ρ^+, or many other objects), the model has a further set of rules and/or parameters to select the precise flavor type. For example, a phenomenologically successful description of the π/ρ ratio is obtained by simply assuming a production rate proportional to the number of spin states (one for the scalar pion, three for the vector rho) and to the Boltzmann factor $\exp(-M/T)$, where M is the resonance mass and T is a universal parameter, to be fit from data. Furthermore, the possibility of converting the potential energy into a diquark–antidiquark pair $(\mathrm{q}_k\mathrm{q}_l)(\bar{\mathrm{q}}_k\bar{\mathrm{q}}_l)$ can be introduced. The resulting hadrons, $\mathrm{q}_i\mathrm{q}_k\mathrm{q}_l$ and $\bar{\mathrm{q}}_j\bar{\mathrm{q}}_k\bar{\mathrm{q}}_l$, are then a baryon–antibaryon pair.

The measurement of hadron multiplicities from Z^0 decays is used to tune the few phenomenological parameters of the model, and these parameters can be used to describe hadronization at different energies and in different high-energy hadron-production processes. The internal consistency of this assumption is supported by Fig. 21 [30], which shows the invariant mass distribution of clusters of color-singlet quarks after the nonperturbative gluon splitting for $\mathrm{e^+e^-}$ collisions at different center-of-mass energies. All curves are normalized to 1, and they all overlap very accurately. This confirms the validity of the implementation of factorization in the Monte Carlo methods: higher initial energies provide more room for the perturbative evolution, leading to more splitting and more emitted radiation; but the structure and distribution of color-singlet clusters at the end of the evolution is independent of the initial energy, and the same model of hadronization can be used.

An example of the quality of the fits to Z^0-decay data is given in Table 1, which is taken from [30]. There, more details are given on the possible variants of the cluster hadronization model and on the choice of parameters used in the fits. Overall, the agreement is excellent!

Excellent agreement is also observed in the kinematic distributions of final-state hadrons [30], in particular, in the

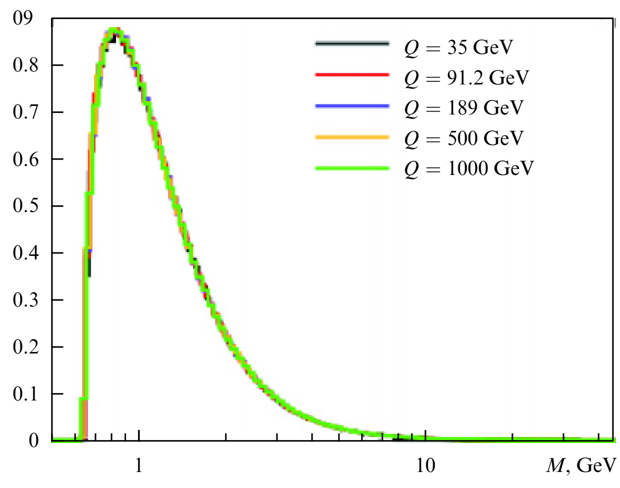

Figure 21. The invariant mass distribution of clusters of colour-singlet quarks after nonperturbative gluon splitting, obtained with the HERWIG generator [30]. The spectra for final states corresponding to different center-of-mass energies are normalized to the same area, displaying the energy independence of the shapes.

fragmentation functions that describe the momentum distribution. This results from the convolution of the momentum spectrum of the partons at the end of the perturbative evolution with momentum smearing due to the hadronization process. Since the latter is independent of the initial scale of the hard scattering, the scale dependence of the fragmentation functions reflects the logarithmic scale dependence of the perturbative evolution, similarly to proton partonic densities.

4. Applications

In hadronic collisions, all phenomena are QCD related. The dynamics are more complex than in the $\mathrm{e^+e^-}$ or deep inelastic scattering because both beam and target have a nontrivial partonic structure. As a result, calculations (and experimental analyses) are more complicated. Perturbative corrections to the Born-level (leading order, or LO) amplitudes require the calculations of a large number of loop and high-order tree-level diagrams. For example, the first correction to the four LO $\mathrm{gg} \to \mathrm{gg}$ diagrams for the jet cross section in the purely gluonic channel requires the evaluation of the one-loop insertions in four LO diagrams, plus the calculation of 25 LO diagrams for the $\mathrm{gg} \to \mathrm{ggg}$ process. Next-to-leading-order (NLO) calculations like this are nevertheless available today for most processes with up to 2 or 3 final-state partons, and new techniques have emerged recently that are pushing the frontier of NLO results even further (see [10] for a recent review). Next-to-next-to-leading order (NNLO) results, which require the evaluation of two-loop corrections as well, have so far been completed for processes with only one final-state particle at the Born level, such as production of massive gauge bosons (W and Z) or of a Higgs boson. For these reasons, the accuracy of QCD calculations in hadronic collisions is typically worse than in the case of $\mathrm{e^+e^-}$ or deep inelastic scattering processes. Nevertheless, $\mathrm{p\bar{p}}$ or $\mathrm{e^+e^-}$ collider physics is primarily *discovery* physics, rather than precision physics (there are exceptions, such as the measurements of the W mass and of the properties of b-hadrons. But these are not QCD-related measurements). As such, knowledge of QCD is essential for both the estimate of the expected signals and the evaluation of the backgrounds. Tests of QCD in $\mathrm{p\bar{p}}$ collisions confirm our understanding of the perturbation theory or, when they fail, point to areas where our approximations need to be improved (see, e.g., the theory advances prompted by the measurements of ψ production at CDF).

In Sections 4.1–4.4, we briefly review some applications to the most commonly studied QCD processes in hadronic collisions: the production of gauge bosons and of jets. More details can be found in Refs [6, 7].

4.1 Drell–Yan processes

While the Z boson has recently been studied with great precision by the LEP experiments, it was actually discovered, together with the W boson, by the CERN experiments UA1 and UA2 in $\mathrm{p\bar{p}}$ collisions. The W physics was studied in great detail at LEP2, but the best direct measurements of its mass by a single group still belong to $\mathrm{p\bar{p}}$ experiments (CDF and D0 at the Tevatron). Until a new, future, $\mathrm{e^+e^-}$ linear collider is built, the monopoly of W studies will remain with hadron colliders, with the Tevatron, and soon with the start of the LHC experiments.

Precision measurements of W production in hadronic collisions are important for several reasons:

Tabl 1. Average particle multiplicities per event in e^+e^- collisions at 91.2 GeV. Experimental data were measured by the following collaborations at LEP and at SLC: ALEPH(A), DELPHI(D), L3(L), OPAL(O), MARK2(M), and SLD(S). The theoretical predictions in the last three columns, taken from Ref. [30], correspond to various implementations of the cluster hadronization model (see Ref. [30] for details).

Particle	Experiment	Measured	Old model	Herwig (C^{++})	Herwig (Fortran)
All charged	M, A, D, L, O	20.924 ± 0.117	20.22*	20.814	20.532*
γ	A, O	21.27 ± 0.6	23.03	22.67	20.74
π^0	A, D, L, O	9.59 ± 0.33	10.27	10.08	9.88
$\rho(770)^0$	A, D	1.295 ± 0.125	1.235	1.316	1.07
$\pi^\pm$	A, O	17.04 ± 0.25	16.30	16.95	16.74
$\rho(770)^\pm$	O	2.4 ± 0.43	1.99	2.14	2.06
η	A, L, O	0.956 ± 0.049	0.886	0.893	0.669*
$\omega(782)$	A, L, O	1.083 ± 0.088	0.859	0.916	1.044
$\eta(958)$	A, L, O	0.152 ± 0.03	0.13	0.136	0.106
K^0	S, A, D, L, O	2.027 ± 0.025	2.121*	2.062	2.026
$K^*(892)^0$	A, D, O	0.761 ± 0.032	0.667	0.681	0.583*
$K^*(1430)^0$	D, O	0.106 ± 0.06	0.065	0.079	0.072
$K^\pm$	A, D, O	2.319 ± 0.079	2.335	2.286	2.250
$K^*(892)^\pm$	A, D, O	0.731 ± 0.058	0.637	0.657	0.578
$\phi(1020)$	A, D, O	0.097 ± 0.007	0.107	0.114	0.134*
p	A, D, O	0.991 ± 0.054	0.981	0.947	1.027
Δ^{++}	D, O	0.088 ± 0.034	0.185	0.092	0.209*
Σ^-	O	0.083 ± 0.011	0.063	0.071	0.071
Λ	A, D, L, O	0.373 ± 0.008	0.325*	0.384	0.347*
Σ^0	A, D, O	0.074 ± 0.009	0.078	0.091	0.063
Σ^+	O	0.099 ± 0.015	0.067	0.077	0.088
$\Sigma(1385)^\pm$	A, D, O	0.0471 ± 0.0046	0.057	0.0312*	0.061*
Ξ^-	A, D, O	0.0262 ± 0.001	0.024	0.0286	0.029
$\Xi(1530)^0$	A, D, O	0.0058 ± 0.001	0.026*	0.0288*	0.009*
Ω^-	A, D, O	0.00125 ± 0.00024	0.001	0.00144	0.0009*
$f_2(1270)$	D, L, O	0.168 ± 0.021	0.113	0.150	0.173
$f_2'(1525)$	D	0.02 ± 0.008	0.003	0.012	0.012
$D^\pm$	A, D, O	0.184 ± 0.018	0.322*	0.319*	0.283*
$D^*(2010)^\pm$	A, D, O	0.182 ± 0.009	0.168	0.180	0.151*
D^0	A, D, O	0.473 ± 0.026	0.625*	0.570*	0.501
$D_s^\pm$	A, O	0.129 ± 0.013	0.218*	0.195*	0.127
$D_s^{*\pm}$	O	0.096 ± 0.046	0.082	0.066	0.043
J/Ψ	A, D, L, O	0.00544 ± 0.00029	0.006	0.00361*	0.002*
Λ_c^+	D, O	0.077 ± 0.016	0.006*	0.023*	0.001*
$\Psi'(3685)$	D, L, O	0.00229 ± 0.00041	0.001*	0.00178	0.0008*

* Indicates a prediction that differs from the measured value by more than three standard deviations.

• This is the only process in hadronic collisions known to the NNLO accuracy.

• The rapidity distribution of the charged leptons from W decays is sensitive to the ratio of the up and down quark densities and can contribute to our understanding of the structure of the proton.

• Deviations from the expected production rates of a highly virtual W ($p\bar{p} \to W^* \to e\nu$) are a possible signal of the existence of new W bosons, and therefore of new gauge interactions. The tail of the invariant mass distribution of the W boson, furthermore, provides today's most sensitive determination of the W width.

The production rate for the W boson is given by the factorization formula

$$\mathrm{d}\sigma(p\bar{p} \to W + X) = \int \mathrm{d}x_1\, \mathrm{d}x_2 \sum_{i,j} f_i(x_1, Q) f_j(x_2, Q) \times \mathrm{d}\hat{\sigma}(ij \to W)\,. \tag{50}$$

The partonic cross section $\hat{\sigma}(ij \to W)$ can be easily calculated, giving the result [5, 6]

$$\hat{\sigma}(q_i\bar{q}_j \to W) = \pi \frac{\sqrt{2}}{3} |V_{ij}|^2 G_F M_W^2\, \delta(\hat{s} - M_W^2) = A_{ij} M_W^2\, \delta(\hat{s} - M_W^2)\,, \tag{51}$$

where $\hat{s}$ is the partonic center-of-mass energy squared and V_{ij} is an element of the Cabibbo–Kobayashi–Maskawa matrix. The delta function comes from the $2 \to 1$ phase space, which forces the center-of-mass energy of the initial state to coincide with the W mass. It is useful to introduce the two variables

$$\tau = \frac{\hat{s}}{S_{\mathrm{had}}} \equiv x_1 x_2\,, \tag{52}$$

$$y = \frac{1}{2}\log\left(\frac{E_W + p_W^z}{E_W - p_W^z}\right) \equiv \frac{1}{2}\log\left(\frac{x_1}{x_2}\right), \tag{53}$$

where S_{had} is the hadronic center-of mass-energy squared. The variable y is called *rapidity*. For slowly moving objects, it reduces to the standard velocity, but in contrast to velocity, it transforms additively under Lorentz boosts along the direction of motion even at high energies. Written in terms of τ and y, the integration measure over the initial-state parton momenta becomes $\mathrm{d}x_1\, \mathrm{d}x_2 = \mathrm{d}\tau\, \mathrm{d}y$. Using this expression

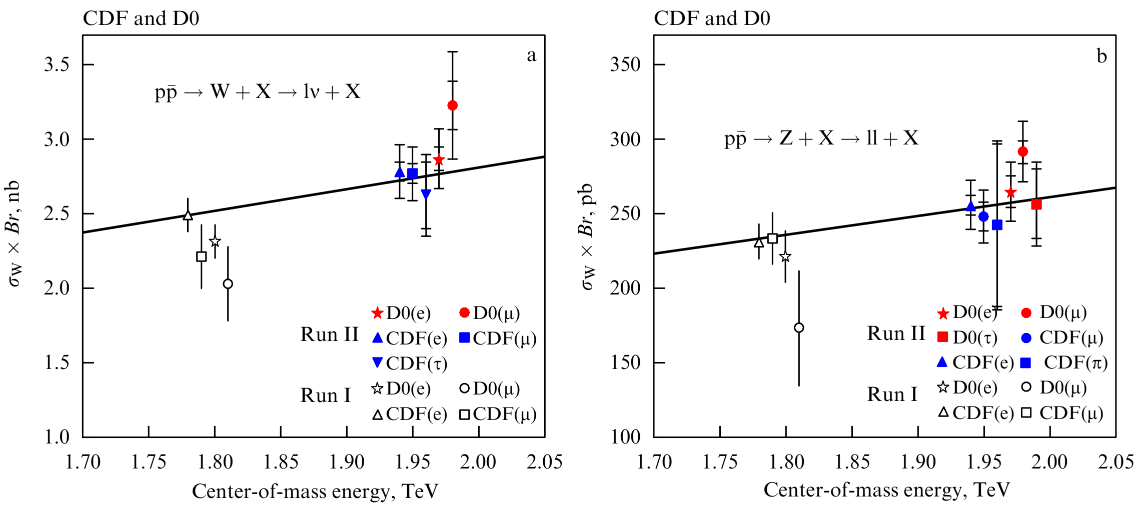

Figure 22. Comparison of the measured $\sigma B(W \to e\nu)$ (a) and $\sigma B(Z^0 \to e^+e^-)$ (b) to 2-loop theoretical predictions.

and Eqn (51) in Eqn (50), we obtain the LO total W production cross section as

$$\sigma_{DY} = \sum_{i,j} \frac{\pi A_{ij}}{M_W^2}\, \tau \int_\tau^1 \frac{dx}{x} f_i(x) f_j\left(\frac{\tau}{x}\right) \equiv \sum_{i,j} \frac{\pi A_{ij}}{M_W^2}\, \tau \mathcal{L}_{ij}(\tau)\,, \tag{54}$$

where the function $\mathcal{L}_{ij}(\tau)$ is usually called the *partonic luminosity*. In the case of $u\bar{d}$ collisions, the overall factor in front of this expression is approximately equal to 6.5 nb. It is interesting to study the partonic luminosity as a function of the hadronic center-of-mass energy. This can be done by taking a simple approximation for the parton densities. Following the indications of the figures presented in the preceding section, we assume that $f_i(x) \sim 1/x^{1+\delta}$ with $\delta < 1$. Then

$$\mathcal{L}(\tau) = \int_\tau^1 \frac{dx}{x} \frac{1}{x^{1+\delta}} \left(\frac{x}{\tau}\right)^{1+\delta} = \frac{1}{\tau^{1+\delta}} \int_\tau^1 \frac{dx}{x} = \frac{1}{\tau^{1+\delta}} \log\left(\frac{1}{\tau}\right), \tag{55}$$

$$\sigma_W \sim \tau^{-\delta} \log\left(\frac{1}{\tau}\right) = \left(\frac{S_{had}}{M_W^2}\right)^\delta \log\left(\frac{S_{had}}{M_W^2}\right). \tag{56}$$

Therefore, the DY cross section increases at least logarithmically with the hadronic center-of-mass energy. This is to be compared with the behavior of the Z production cross section in e^+e^- collisions, which is steeply decreasing for values of s well above the production threshold. The reason for the different behavior in hadronic collisions is that while the energy of the hadronic initial state increases, it is always possible to find partons inside the hadrons with the appropriate energy to produce the W boson directly on shell. The number of partons available for the production of a W boson increases with an increase in the hadronic energy, since the larger the hadron energy is, the smaller the value of hadron momentum fraction x necessary to produce the W boson. The increasing number of partons available at smaller and smaller values of x then causes an increase in the total W production cross section.

A comparison between the best available predictions for the production rates of W and Z bosons in hadronic collisions [31] and the experimental data is shown in Fig. 22. The experimental uncertainties will soon be dominated by the limited knowledge of the machine luminosity, and will exceed the accuracy of the NNLO predictions. This suggests that at the LHC, the total rate of produced W and Z bosons could be used as an accurate luminometer.

The excellent agreement between theory and data extends, albeit with a lower statistical significance, to a comparison of cross sections for the production of multiple gauge bosons, like $W\gamma$, $Z\gamma$, WW, WZ, and ZZ, as shown in Fig. 23.

It is also interesting to note that an accurate measurement of the relative W and Z production rates (which is not affected by the knowledge of the total integrated luminosity, which cancels in their ratio) provides a tool to measure the total W width. This can be seen from the equation

$$\Gamma_W = \underbrace{\frac{N^{obs}(Z \to e^+e^-)}{N^{obs}(W \to e^\pm\nu)}}_{\text{measure}} \underbrace{\left(\frac{\sigma_{W^\pm}}{\sigma_Z}\right)}_{\text{calculable}} \underbrace{\left(\frac{\Gamma^W_{e\nu}}{\Gamma^Z_{e^+e^-}}\right)}_{\text{calculable}} \underbrace{\Gamma_Z}_{\text{LEP/SLC}}\,.$$

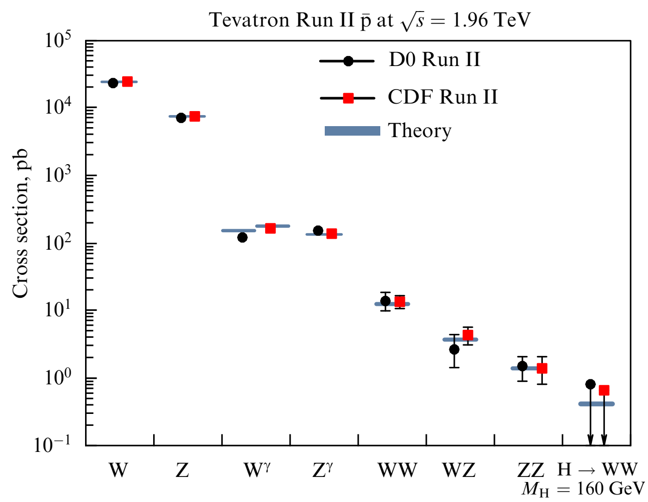

Figure 23. Comparison of electroweak cross sections measured at the Tevatron [32] and theoretical calculations.

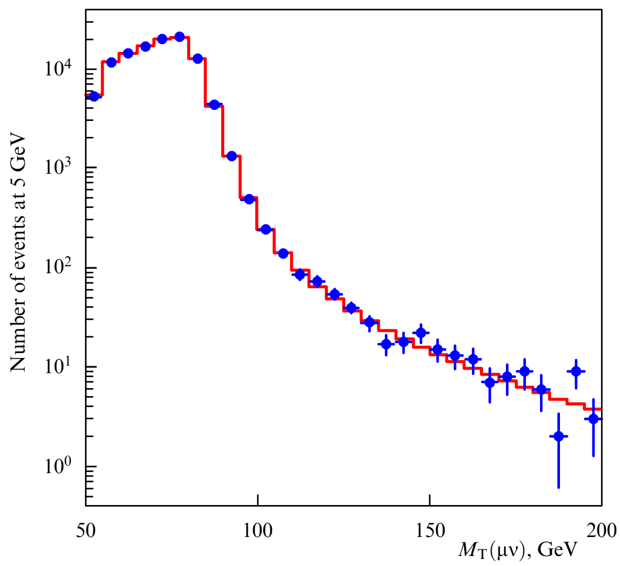

Figure 24. The transverse mass distribution of the W boson in its $\mu\nu$ final state, used to extract the W width.

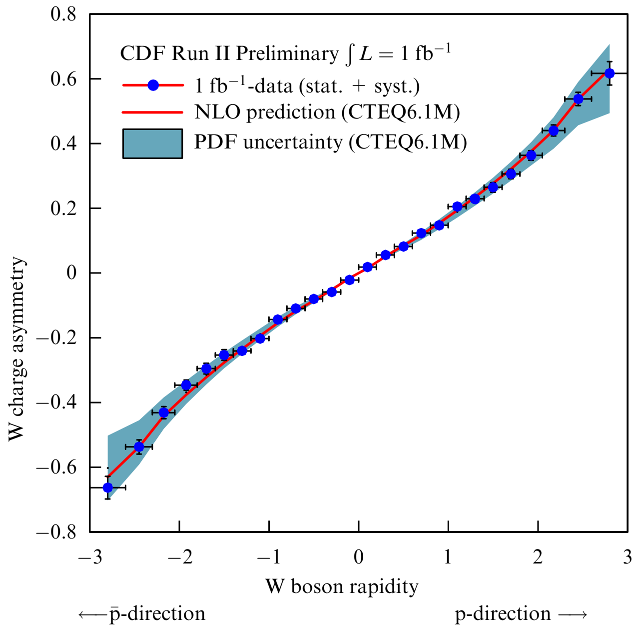

Figure 25. The rapidity spectrum of the W^+ boson produced at the Tevatron, from which the W rapidity asymmetry $A(y)$ is extracted.

The use of this formula for an indirect extraction of the W width, combining the results of the CDF and D0 experiments [33], leads to $\Gamma_W = 2141 \pm 57$ MeV. With the large body of statistics available today at the Tevatron, the W width can also be determined *directly* by probing the tails of the Breit–Wigner distribution, which gives rise to very off-mass-shell $W^* \to l\nu_l$ final states. The high-mass tail, shown in Fig. 24 in the case of muonic final states, leads to $\Gamma_W = 2032 \pm 73$ MeV [34]. The combination of this measurement with previous ones and with a preliminary D0 result gives $\Gamma_W = 2056 \pm 58$ MeV [35].

4.2 W rapidity asymmetry

The measurement of the charge asymmetry in the rapidity distribution of W bosons produced in $p\bar{p}$ collisions can provide an important measurement of the ratio of the u-quark and d-quark momentum distributions. Using the formulas given above, it can be easily verified as an exercise that

$$\frac{d\sigma_{W^+}}{dy} \propto f_u^p(x_1) f_{\bar{d}}^{\bar{p}}(x_2) + f_{\bar{d}}^p(x_1)\, f_u^{\bar{p}}(x_2)\,, \tag{57}$$

$$\frac{d\sigma_{W^-}}{dy} \propto f_{\bar{u}}^p(x_1)\, f_d^{\bar{p}}(x_2) + f_d^p(x_1)\, f_{\bar{u}}^{\bar{p}}(x_2)\,. \tag{58}$$

We can then construct the following charge asymmetry (assuming the dominance of the quark densities over the antiquark ones, which is valid in the kinematical region of interest for W production at the Tevatron):

$$A(y) = \frac{d\sigma_{W^+}/dy - d\sigma_{W^-}/dy}{d\sigma_{W^+}/dy + d\sigma_{W^-}/dy}$$
$$= \frac{f_u^p(x_1) f_d^p(x_2) - f_d^p(x_1) f_u^p(x_2)}{f_u^p(x_1) f_d^p(x_2) + f_d^p(x_1) f_u^p(x_2)}\,. \tag{59}$$

Setting $f_d(x) = f_u(x)\, R(x)$, we then obtain

$$A(y) = \frac{R(x_2) - R(x_1)}{R(x_2) + R(x_1)}\,, \tag{60}$$

which measures the $R(x)$ ratio, since $x_{1,2}$ are known in principle from the kinematics: $x_{1,2} = \sqrt{\tau}\exp(\pm y)$. It is impossible to determine $x_{1,2}$ with arbitrary precision on an event-by-event basis because the longitudinal momentum of the neutrino cannot be measured to better than a twofold degeneracy, corresponding to W with two different rapidity values. Associating a weight with the two possible solutions of the kinematics such that the weight is proportional to the cross section nevertheless allows the W extraction to be done statistically, and the large data samples available today at the Tevatron allow rather accurate measurements. In fact, the current CDF and D0 data have become more accurate than the uncertainty associated with available PDF fits, as shown in Fig. 25, taken from a preliminary CDF result [36]. This measurement will therefore provide an important additional constraint in the determination of the quark densities.

4.3 Jet production

Jet production is the hard process with the largest rate in hadronic collisions. For example, the cross section for producing jets of transverse energy $E_T^{\text{jet}} \gtrsim 50$ GeV at the Tevatron ($\sqrt{S_{\text{had}}} = 1.96$ TeV) is of the order of a μb, meaning $\sim 10^4$ events/s at the luminosities available at the Tevatron. The data collected at the Tevatron have so far extended up to the E_T values of the order of 600 GeV. These events are generated by collisions among partons that carry over 60% of the available $p\bar{p}$ energy and allow probing the shortest distances ever reached. The leading mechanisms for jet production are shown in Fig. 26.

The 2-jet inclusive cross section can be obtained from the formula

$$d\sigma = \sum_{ijkl} dx_1\, dx_2 f_i^{(H_1)}(x_1, \mu) f_j^{(H_2)}(x_2, \mu)\, \frac{d\hat{\sigma}_{ij\to k+l}}{d\Phi_2}\, d\Phi_2\,, \tag{61}$$

which has to be expressed in terms of the rapidity and transverse momentum of the quarks (or jets) in order to

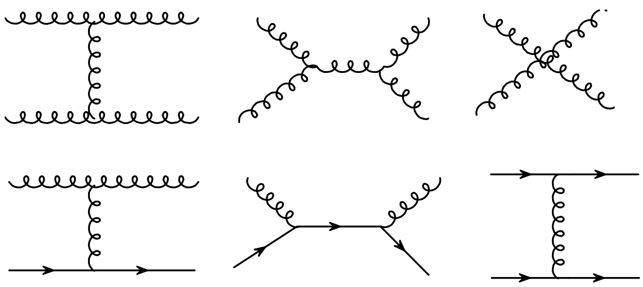

Figure 26. Representative diagrams for the production of jet pairs in hadronic collisions.

make contact with physical reality. The two-particle phase space is given by

$$\mathrm{d}\Phi_2 = \frac{\mathrm{d}^3 k}{2k^0 (2\pi)^3}\, 2\pi\, \delta\big((p_1 + p_2 - k)^2\big)\,, \tag{62}$$

and in the center-of-mass system of the colliding partons, we obtain

$$\mathrm{d}\Phi_2 = \frac{1}{2(2\pi)^2}\, \mathrm{d}^2 k_\mathrm{T}\, \mathrm{d}y\, 2\, \delta\big(\hat{s} - 4(k^0)^2\big)\,, \tag{63}$$

where k_T is the transverse momentum of the final-state partons and y is the rapidity of the produced parton in the parton center-of-mass frame, given by

$$y = \frac{y_1 - y_2}{2}\,, \tag{64}$$

where y_1 and y_2 are the rapidities of the produced partons in the laboratory frame (in fact, in any frame). We also introduce

$$y_0 = \frac{y_1 + y_2}{2} = \frac{1}{2}\log\frac{x_1}{x_2}\,, \qquad \tau = \frac{\hat{s}}{S_\mathrm{had}} = x_1 x_2\,, \tag{65}$$

such that

$$\mathrm{d}x_1\, \mathrm{d}x_2 = \mathrm{d}y_0\, \mathrm{d}\tau\,. \tag{66}$$

We obtain

$$\mathrm{d}\sigma = \sum_{ijkl} \mathrm{d}y_0\, \frac{1}{S_\mathrm{had}}\, f_i^{(\mathrm{H}_1)}(x_1, \mu) \times f_j^{(\mathrm{H}_2)}(x_2, \mu)\, \frac{\mathrm{d}\hat{\sigma}_{ij\to k+l}}{\mathrm{d}\Phi_2}\, \frac{1}{2(2\pi)^2}\, 2\, \mathrm{d}y\, \mathrm{d}^2 k_\mathrm{T}\,, \tag{67}$$

which can also be written as

$$\frac{\mathrm{d}\sigma}{\mathrm{d}y_1\, \mathrm{d}y_2\, \mathrm{d}^2 k_\mathrm{T}} = \frac{1}{S_\mathrm{had}\, 2(2\pi)^2} \sum_{ijkl} f_i^{(\mathrm{H}_1)}(x_1, \mu) \times f_j^{(\mathrm{H}_2)}(x_2, \mu)\, \frac{\mathrm{d}\hat{\sigma}_{ij\to k+l}}{\mathrm{d}\Phi_2}\,. \tag{68}$$

The variables x_1 and x_2 can be obtained from y_1, y_2, and k_T using the equations

$$y_0 = \frac{y_1 + y_2}{2}\,, \tag{69}$$

$$y = \frac{y_1 - y_2}{2}\,, \tag{70}$$

$$x_\mathrm{T} = \frac{2k_\mathrm{T}}{\sqrt{S_\mathrm{had}}}\,, \tag{71}$$

$$x_1 = x_\mathrm{T} \exp(y_0) \cosh y\,, \tag{72}$$

$$x_2 = x_\mathrm{T} \exp(-y_0) \cosh y\,. \tag{73}$$

For the partonic variables, we need $\hat{s}$ and the scattering angle in the parton center-of-mass frame θ because

$$t = -\frac{\hat{s}}{2}(1 - \cos\theta)\,, \qquad u = -\frac{\hat{s}}{2}(1 + \cos\theta)\,. \tag{74}$$

Neglecting the parton masses, it can be shown that the rapidity can also be written as

$$y \approx -\log\tan\frac{\theta}{2} \equiv \eta\,, \tag{75}$$

with η usually being referred to as pseudorapidity.

The leading-order Born cross sections for parton–parton scattering are reported in Table 2.

It is interesting to note that a good approximation to the exact results can easily be obtained by using the soft-gluon techniques introduced before. Based on the fact that even at 90°, $\min(|t|, |u|)$ does not exceed $s/2$, and therefore, all else being equal, a propagator in the t or u channel contributes to the square of an amplitude 4 times more than a propagator in the s channel, it is reasonable to assume that the amplitudes are dominated by the diagrams with a gluon exchanged in the t (or u) channel. It is easy to calculate the amplitudes in this limit using the soft-gluon approximation. For example, the amplitude for the exchange of a soft gluon in a qq' pair is given by

$$(\lambda^a_{ij})(\lambda^a_{kl})\, 2p_\mu\, \frac{1}{t}\, 2p'_\mu = \lambda^a_{ij}\lambda^a_{kl}\, \frac{4pp'}{t} = \frac{2s}{t}\, \lambda^a_{ij}\lambda^a_{kl}\,. \tag{76}$$

Table 2. Cross sections for light parton scattering. The notation is $p_1 p_2 \to kl$, $\hat{s} = (p_1 + p_2)^2$, $\hat{t} = (p_1 - k)^2$, and $\hat{u} = (p_1 - l)^2$.

Process	$\dfrac{\mathrm{d}\hat{\sigma}}{\mathrm{d}\Phi_2}$
$\mathrm{qq}' \to \mathrm{qq}'$	$\frac{1}{2\hat{s}}\frac{4}{9}\frac{\hat{s}^2 + \hat{u}^2}{\hat{t}^2}$
$\mathrm{qq} \to \mathrm{qq}$	$\frac{1}{2}\frac{1}{2\hat{s}}\left[\frac{4}{9}\left(\frac{\hat{s}^2 + \hat{u}^2}{\hat{t}^2} + \frac{\hat{s}^2 + \hat{t}^2}{\hat{u}^2}\right) - \frac{8}{27}\frac{\hat{s}^2}{\hat{u}\hat{t}}\right]$
$\mathrm{q\bar{q}} \to \mathrm{q'\bar{q}'}$	$\frac{1}{2\hat{s}}\frac{4}{9}\frac{\hat{t}^2 + \hat{u}^2}{\hat{s}^2}$
$\mathrm{q\bar{q}} \to \mathrm{q\bar{q}}$	$\frac{1}{2\hat{s}}\left[\frac{4}{9}\left(\frac{\hat{s}^2 + \hat{u}^2}{\hat{t}^2} + \frac{\hat{t}^2 + \hat{u}^2}{\hat{s}^2}\right) - \frac{8}{27}\frac{\hat{u}^2}{\hat{s}\hat{t}}\right]$
$\mathrm{q\bar{q}} \to \mathrm{gg}$	$\frac{1}{2}\frac{1}{2\hat{s}}\left[\frac{32}{27}\frac{\hat{t}^2 + u^2}{\hat{t}\hat{u}} - \frac{8}{3}\frac{\hat{t}^2 + \hat{u}^2}{\hat{s}^2}\right]$
$\mathrm{gg} \to \mathrm{q\bar{q}}$	$\frac{1}{2\hat{s}}\left[\frac{1}{6}\frac{\hat{t}^2 + \hat{u}^2}{\hat{t}\hat{u}} - \frac{3}{8}\frac{\hat{t}^2 + \hat{u}^2}{\hat{s}^2}\right]$
$\mathrm{gq} \to \mathrm{gq}$	$\frac{1}{2\hat{s}}\left[-\frac{4}{9}\frac{\hat{s}^2 + \hat{u}^2}{\hat{s}\hat{u}} + \frac{\hat{u}^2 + \hat{s}^2}{\hat{t}^2}\right]$
$\mathrm{gg} \to \mathrm{gg}$	$\frac{1}{2}\frac{1}{2\hat{s}}\frac{9}{2}\left(3 - \frac{\hat{t}\hat{u}}{\hat{s}^2} - \frac{\hat{s}\hat{u}}{\hat{t}^2} - \frac{\hat{s}\hat{t}}{\hat{u}^2}\right)$

The p_μ and p'_μ factors represent the coupling of the exchanged gluon to the q and q$'$ quark lines [see Eqn (36)]. Squaring, and summing and averaging over spins and colors gives

$$\overline{\sum}_{\text{colors, spin}} |M_{qq'}|^2 = \frac{1}{N^2}\left(\frac{N^2-1}{4}\right)\frac{4s^2}{t^2} = \frac{8}{9}\frac{s^2}{t^2}\,. \qquad (77)$$

Because the diagram for this process with a t-channel gluon exchange is symmetric under the $s \leftrightarrow u$ exchange, and because $u \to -s$ in the $t \to 0$ limit, the above result can be rewritten in an explicitly s, u symmetric way as

$$\frac{4}{9}\frac{s^2+u^2}{t^2}\,, \qquad (78)$$

which indeed exactly agrees with the result of the exact calculation given in Table 2. The corrections that appear from the s or u gluon exchange when the quark flavors are the same or when we study a q$\bar{\text{q}}$ process are small, as can be seen by comparing the above result with the expressions in the table.

As another example, we consider the case of qg $\to$ qg scattering. The amplitude is exactly the same as in the qq$'$ $\to$ qq$'$ case, up to different color factors. A simple calculation then gives

$$\overline{\sum}_{\text{colors, spin}} |M_{qg}|^2 = \frac{9}{4}\overline{\sum}|M_{qq'}|^2 = \frac{s^2+u^2}{t^2}\,. \qquad (79)$$

The exact result is

$$\frac{u^2+s^2}{t^2} - \frac{4}{9}\frac{u^2+s^2}{us} \qquad (80)$$

which, even at the point $\theta = 90°$ where the t-channel exchange approximation is the worst, differs from (79) by no more than 25%.

As a final example, we consider the case of gg $\to$ gg scattering, which in our approximation gives

$$\overline{\sum}|M_{gg}|^2 = \frac{9}{2}\frac{s^2}{t^2}\,. \qquad (81)$$

Based on the $u \leftrightarrow t$ symmetry, we should expect the simple improvement

$$\overline{\sum}|M_{gg}|^2 \sim \frac{9}{2}\left(\frac{s^2}{t^2}+\frac{s^2}{u^2}\right). \qquad (82)$$

This only differs by 20% from the exact result at $\theta = 90°$.

We note that the relation

$$\hat{\sigma}_{gg} : \hat{\sigma}_{qg} : \hat{\sigma}_{q\bar{q}} = \left(\frac{9}{4}\right) : 1 : \left(\frac{4}{9}\right) \qquad (83)$$

holds at small t. The 9/4 factors are simply the ratios of the color factors for the coupling to gluons of a gluon (C_A) and of a quark (T_F), after including the respective color-average factors $1/(N^2-1)$ for the gluon and $1/N$ for the quark. Using Eqn (83), we can then write

$$\begin{aligned} d\sigma_{\text{hadr}} &= \int dx_1\, dx_2 \sum_{i,j} f_i(x_1) f_j(x_2)\, d\hat{\sigma}_{ij} \\ &= \int dx_1\, dx_2\, F(x_1)\, F(x_2)\, d\hat{\sigma}_{gg}(gg \to \text{jets})\,, \end{aligned} \qquad (84)$$

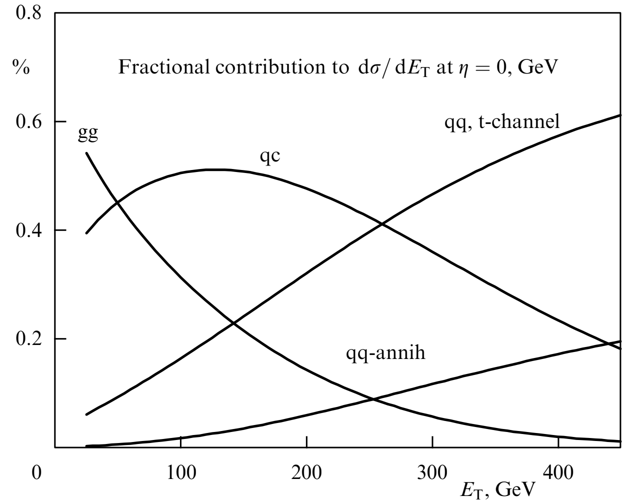

Figure 27. Relative contribution to the inclusive jet-E_T rates from the different production channels.

where the object

$$F(x) = f_g(x) + \frac{4}{9}\sum_f \left[q_f(x) + \bar{q}_f(x)\right] \qquad (85)$$

is usually called the *effective structure function*. This result indicates that the measurement of the inclusive jet cross section does not in principle allow disentangling the independent contribution of the various partonic components of the proton, unless of course a kinematic region is considered where the production is dominated by a single process. The relative contributions of the different channels calculated using current fits of parton densities are shown for the Tevatron collider at 1.8 TeV in Fig. 27.

4.4 Comparison of theory and experimental data

Predictions for jet production at colliders are available today at the next-to-leading order in QCD (see the review in Ref. [7]). One of the preferred observables is the inclusive E_T spectrum. An accurate comparison of data and theory, should it exhibit discrepancies at the largest values of E_T, could provide evidence for new phenomena, such as the existence of a quark substructure.

For years, it has been known [37] that an underlying quark compositeness would increase the rate of the highest-E_T jets. The real question, therefore, is how we convince ourselves that the prediction is indeed *accurate*. This question became particularly relevant in 1995, when the CDF collaboration measured a jet cross section that appeared to deviate from theory in precisely the way predicted by an underlying quark compositeness (see Fig. 28). How do we know that this is not due to poorly known quark or gluon densities at large x? In principle, we could incorporate the CDF jet data into a global fit to the partonic PDFs and verify whether it is possible to modify them so as to maintain agreement with the other data, and at the same time to also satisfactorily fit the jet data themselves. On the other hand, doing this would prevent us from using the jet spectrum as a probe of new physics. In other words, we might be hiding away a possible signal of new physics by ascribing it to the PDFs.

Is it possible to have a complementary determination of the PDF at high x that could constrain the possible PDF

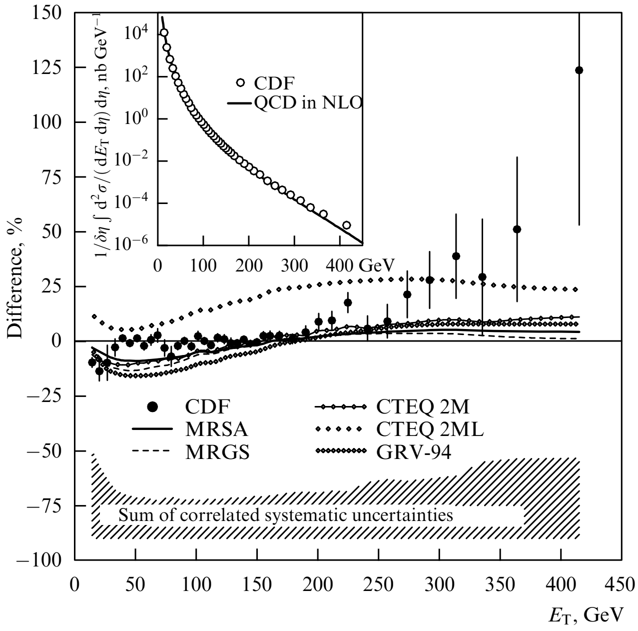

Figure 28. Comparison of the data and theory in an early measurement of the jet cross section at the Tevatron by the CDF experiment [38].

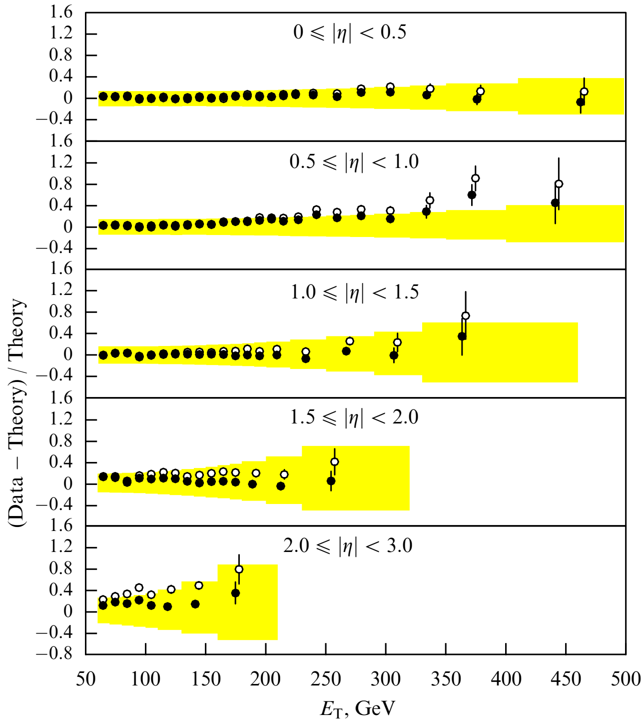

Figure 29. Inclusive E_T spectra for jets in different rapidity regions, measured at the run 1 of the Tevatron by the D0 Collaboration [39].

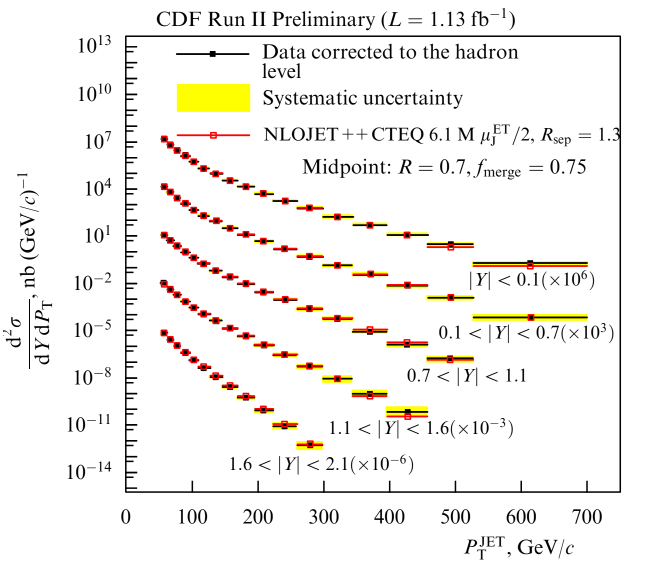

Figure 30. Inclusive jet E_T spectra measured for various rapidity ranges by the CDF experiment at the Tevatron [41], compared to NLO QCD calculations.

systematics of the jet cross section and simultaneously leave the high-E_T tail as an independent and usable observable? This is indeed possible, by fully exploiting the kinematics of dijet production and the wide rapidity coverage of the collider detectors. In fact, final states could be considered where the dijet system is highly boosted in the forward or backward region, for example, the cases where $x_1 \to 1$ and $x_2 \ll 1$. The invariant mass of the dijet system would then be small (because $M_{jj}^2 = x_1 x_2 S \ll S$), and we know from lower-energy measurements that at this scale, jets must behave like pointlike particles, following exactly the QCD-predicted rate. These final states are characterized by having jets at large positive rapidity. We could therefore perform a measurement with forward jets and use these data to fit the $x_1 \to 1$ behavior of the quark and gluon PDFs without the risk of washing away possible new-physics effects. At that point, the large-x PDFs thus constrained can be safely applied to the kinematic configurations where both x_1 and x_2 are large (the highest-E_T final states), and if any residual discrepancy between data and theory is observed, infer the possible presence of new physics.

In the case of the Tevatron data, the study of the forward-jet configurations was performed by the D0 collaboration [39]. Figure 29, from that work, shows the comparison between data and theory for different jet-rapidity intervals. Two different PDF sets are used, CTEQ4M and CTEQ4HJ [40], the latter having been tuned to describe the CDF high-E_t jet tail. We note the good overall agreement of this prediction for the whole set of rapidities. After this tuning, the residual discrepancy between the CDF high-E_T data and QCD is within the theoretical and experimental systematic uncertainties, confirming that jets behave as is expected in the Standard Model. This conclusion has been strengthened by the analysis of the run-2 data [41, 42] at $\sqrt{S} = 1.96$ TeV, as shown in Figs 30 and 31. At this center-of-mass energy, jets up to 600 GeV in transverse momentum have been observed, which means $x \gtrsim 0.6$ and $Q^2 \simeq 400000$ GeV^2. The current agreement between theory and data is excellent over 8 orders of magnitude of cross section, from $E_T \sim 50$ GeV to $E_T \sim 600$ GeV. The experimental and theoretical systematic uncertainties, however, become larger than 30% when $E_T \gtrsim 400$ GeV, preventing a very accurate test of the smallest scales. More data on jet production at large rapidity will allow reducing the PDF uncertainties at large x. However, the uncertainty in the absolute energy scale remains a critical experimental limitation that is difficult to overcome at the highest energies. This will be even more true at the LHC, where jets with energies up to 4 TeV will be detected and studied.

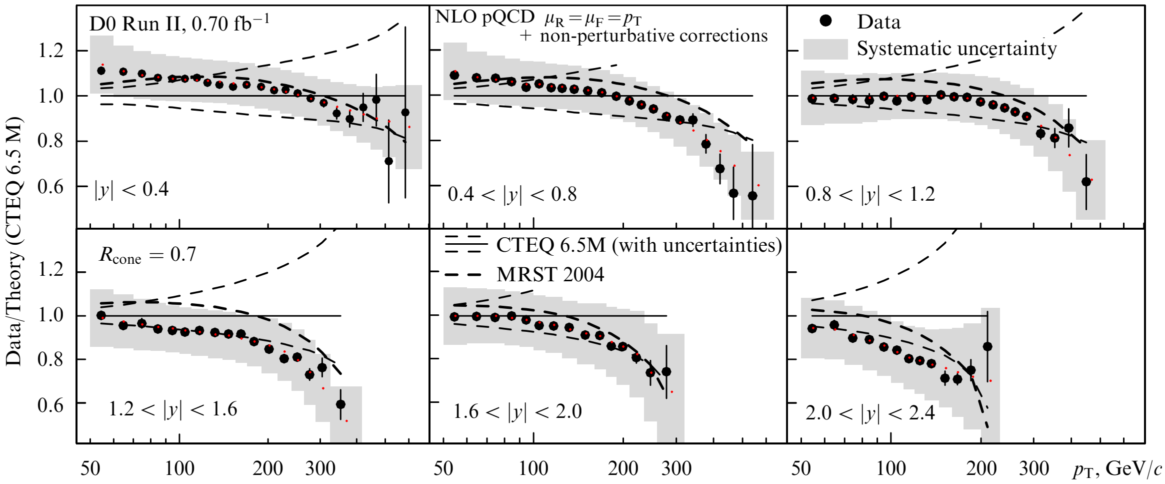

Figure 31. Comparison of run-2 inclusive jet cross sections by the D0 collaboration [42] with QCD calculations. The dashed lines represent the systematics band due to PDF uncertainties.

The $t\bar{t}$ production has been well tested at the Tevatron [43, 44]. Theoretical NLO calculations, enhanced by the resummation of leading and subleading Sudakov logarithms [45], correctly predict the total cross section, as is shown in Fig. 32. The predictions for the LHC are expected to be equally accurate, if not better, because the main source of uncertainty, the PDFs, fall at the LHC in a range of x values where they are known with a higher precision than at the Tevatron. The kinematic production properties, such as the transverse momentum distribution or the invariant mass of the $t\bar{t}$ pair, are also well described by theory, and Monte Carlo event generators are available to model the full structure of the final states, including both the full set of NLO corrections [49] and the emission of multiple extra jets [50], which is relevant for the backgrounds to supersymmetry.

The W+jets and Z+jets processes are very similar from the standpoint of QCD. There are minor differences related to the possibly different initial-state flavor compositions, but the main theoretical systematics, coming from the renormalization-scale sensitivity due to the lack of higher-order perturbative corrections, are strongly correlated.

In the case of W/Z + 1 and W/Z + 2 jets, parton-level NLO calculations are available [51]. They are in excellent agreement with the measurements at the Tevatron [52, 53], as demonstrated, for example, in the case of Z + 1 and Z + 2 jets by the CDF results [52] shown in Fig. 33. Going to higher jet multiplicities and generating a realistic representation of the fully hadronic final state is then possible with LO calculations.

Exact LO matrix element calculations of multiparton production can be enhanced by merging with shower Monte

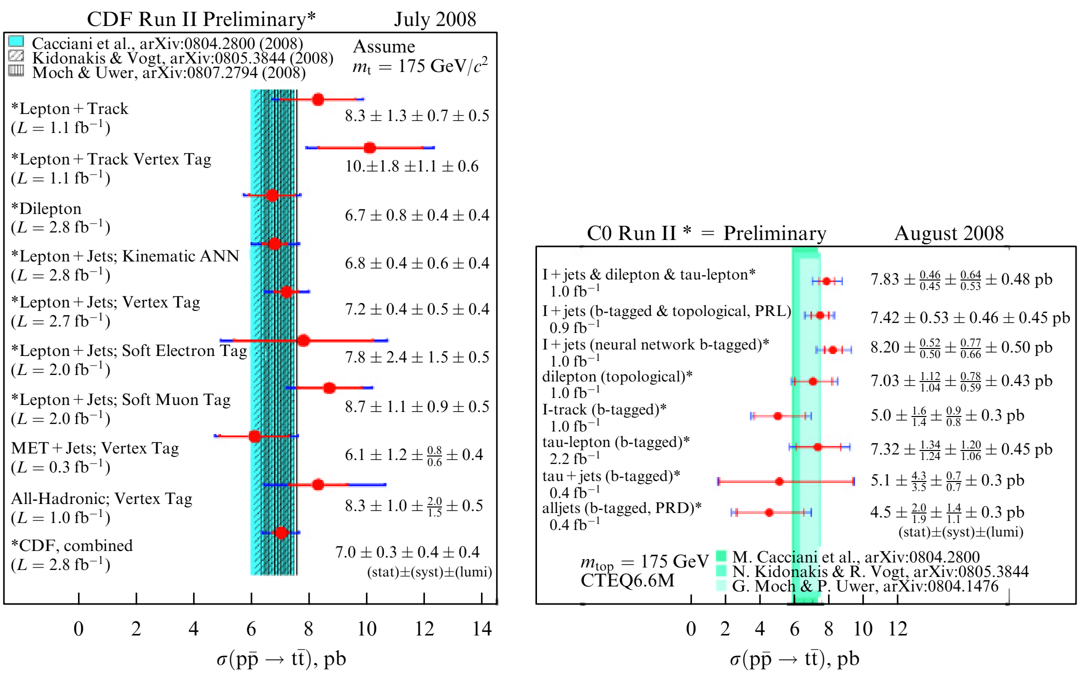

Figure 32. Measurements of the $t\bar{t}$ production cross sections at the Tevatron [43, 44] compared with the state-of-the-art QCD predictions [46–48] (shadowed band).

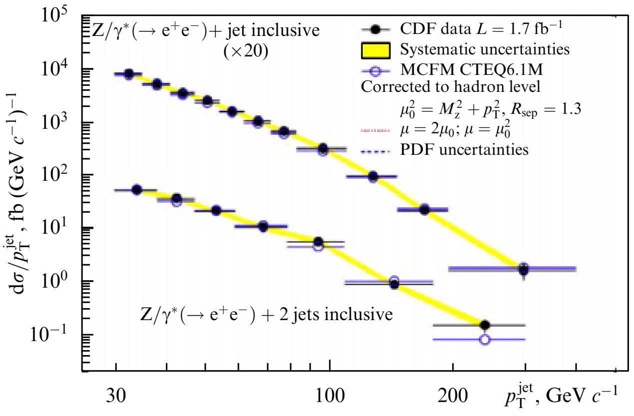

Figure 33. Jet E_T spectra in Z+ measured by the CDF collaboration at the Tevatron [52].

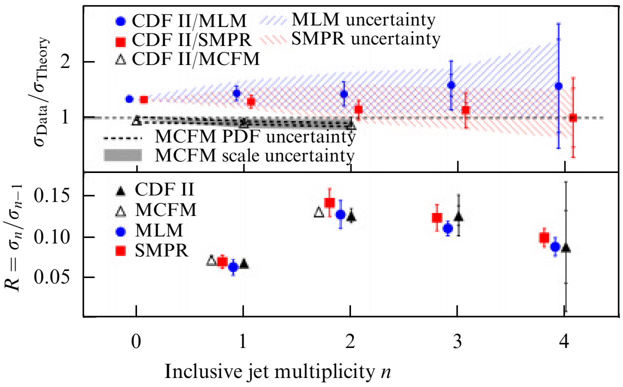

Figure 34. Comparison between CDF data and theory for W + N-jet cross sections [54].

Carlo codes, which add the full perturbative gluon shower and eventual hadronization. An example of the quality of these predictions is given by Fig. 34, which shows the ratio of the measured [54] and predicted W + N jet cross sections, for jets with $E_T > 25$ GeV. The theoretical predictions include the LO results from Ref. [55] (labeled as MLM) and from Ref. [56] (labeled as SMPR), while MCFM refers to the NLO predictions for the 1- and 2-jet rates from Ref. [51]. The systematic uncertainties of the individual calculations, mostly due to the choice of renormalization scale, are shown. The LO results, which have an absolute normalization for all N-jet values, are in good agreement with the data, up to an overall K factor of the order of 1.4. The prediction for the ratios of the N-jet and $(N-1)$-jet rates is also in good agreement with the data. The NLO calculations embody the K factor and exactly reproduce the 1- and 2-jet rates.

Thorough comparisons have been performed [57] among a set of independent calculations of W+ multijet final states [55, 58–61]. The results of the matrix element evaluation for these complex processes are all in excellent agreement; differences in the predictions at the level of hadrons may instead arise from the use of different parton-shower approaches and of different ways of sharing between matrix elements and the shower describing the radiation of hard jets. An example of the spread in the predictions is shown in Fig. 35, which shows the E_T spectra of the four highest-E_T jets in W+ multijet events at the LHC. With the exception of the predictions from one of the codes, all results are within ±50% of each other, an accuracy that will be improved by tuning the parameters of the various calculations once the data are available. The size of these differences is compatible with the intrinsic uncertainties of the calculations, given, for example, by the size of the bands in Fig. 34. It is expected that they can be removed by tuning the input parameters, like the choice of renormalization scale, by fitting the data. An accurate determination of the normalization and shape of the Standard Model background to a supersymmetric signal could therefore be obtained by analyzing data control samples. The description of the $(Z \to \nu\bar{\nu})$+ jets process can be validated, and the absolute normalization of the rate can be tuned by measuring the signal-free $(Z \to e^+e^-)$+ jets final states. This information can then be directly used to tune the W+ jets predictions; the $(W \to e\nu)$+ jets can be measured directly in a region where the electron is clearly tagged, with the resulting tuning used to extrapolate to the case of τ decays, or to decays where the e and μ are not detected. That the calculations appear to well reproduce the ratios of $\sigma[N\text{-jet}]/\sigma[(N-1)\text{-jet}]$ provides a further handle.

A clear path is therefore available to establish the accuracy of the theoretical tools and to provide robust background estimates for searches of anomalies in the multijet plus E_T final states, which, together with the production of top quarks and of inclusive jets, provide the largest backgrounds to searches for a large fraction of the anticipated new phenomena that might be uncovered by the LHC. Presently, there is no reason to doubt that the state of predictions for the LHC is in very good shape, and that no major surprise should emerge. As always, however, the devil is in the details. As shown by the Tevatron analyses, even the measurement of the background W+ multijet cross sections is not an easy task, due to a large contamination from $b\bar{b}$ backgrounds (where both b-hadrons decay semileptonically, one giving rise to a hard and isolated charged lepton and the other to a very energetic neutrino), and $t\bar{t}$ backgrounds, which at the LHC are the dominant source of W+ multijet events. It is therefore difficult to anticipate the dimension of the challenge: only direct contact with data will tell!

5. Conclusions

In spite of the intrinsic complexity of the proton, the factorization framework allows a complete, accurate, and successful description of the rates and properties of hard processes in hadronic collisions. One of the key ingredients of this formulation is the universality of the phenomenological parameterizations of the various nonperturbative components of the calculations (the partonic densities and the hadronization phase). This universality allows extracting the nonperturbative information from the comparison of data and theory in a set of benchmark measurements and applying this knowledge to different observables, or to different experimental environments. All the differences are then to be accounted for by the purely perturbative part of the evolution.

Many years of experience at the Tevatron collider, at HERA, and at LEP have led to an immense improvement in our understanding and to the validation of this framework, and put us today in a solid position to reliably anticipate the features of LHC final states in quantitative terms. LEP, in addition to testing the electroweak interaction sector with great accuracy, has verified the predictions of perturbative QCD at the percent level, from the running of the strong

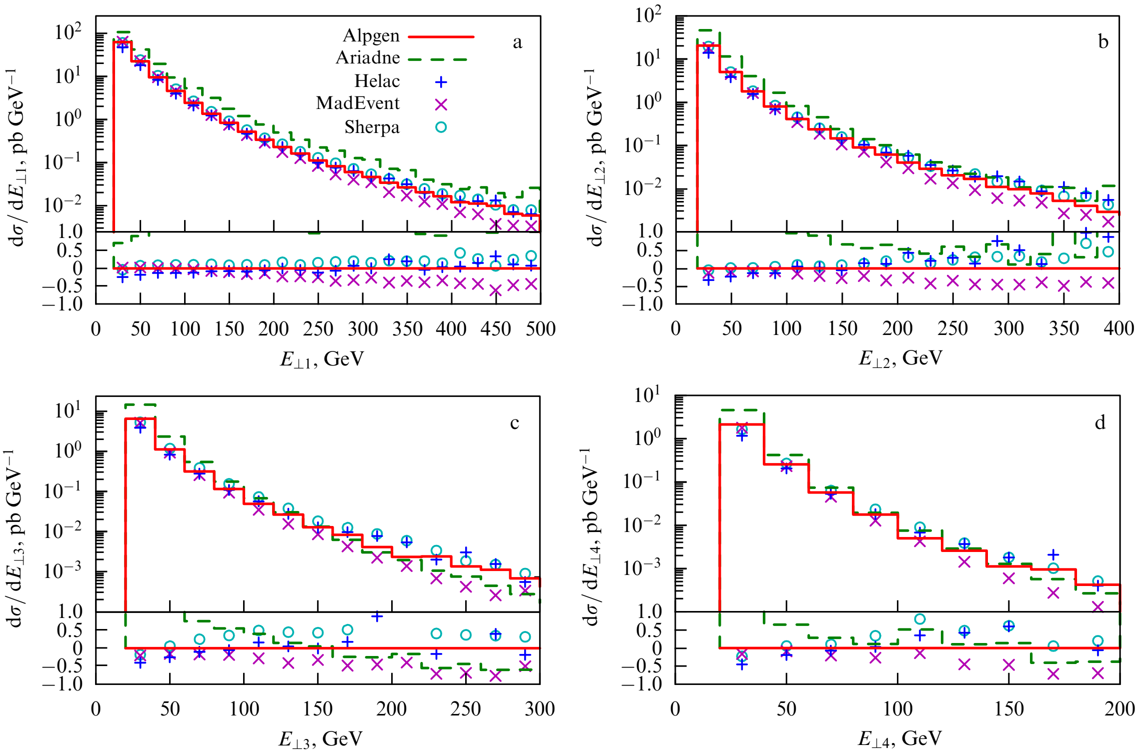

Figure 35. Predicted jet E_T spectra in W+jet(s) final states at the LHC [57].

coupling constant to the description of the perturbative evolution of single quarks and gluons, down to the nonperturbative boundary where strong interactions take over and cause the confinement of partons into hadrons. The description of this transition, relying on the factorization theorem that allows consistently separating the perturbative and nonperturbative phases, has been validated by the study of LEP data at various energies and their comparison with data from lower-energy e^+e^- colliders, which allowed determining the phenomenological parameters introduced to model hadronization. The factorization theorem supports the use of these parameters for the description of the hadronization transition in other experimental environments. HERA has made it possible to probe the short-distance properties of the proton with great accuracy, with the measurement of its partonic content over a broad range of momentum fractions x. These inputs, from LEP and from HERA, beautifully merge into the tools that have been developed to describe proton–antiproton collisions at the Tevatron, where the agreement between theoretical predictions and data confirms that the key assumptions of the overall approach are robust.

The accuracy of the perturbative input relies on complete higher-order calculations and possible resummations of the leading contributions to all orders of the perturbation theory. Today's theoretical precision varies from the few percent level of W and Z inclusive cross sections, which are known to the next-to-next-to-leading order, to the level of 10% for several processes known to the next-to-leading-order (inclusive jet cross sections, top quark production, production of pairs of electroweak gauge bosons), up to very crude estimates for the most complex, multijet final states, where uncertainties at the available leading order can be higher than factors of 2. When these uncertainties are combined with the uncertainties of the nonperturbative inputs, e.g., of the parton densities, the theoretical predictions give very good agreement with all data from the Tevatron collider. In several examples, the theoretical accuracy cannot unfortunately be challenged by the measurements, whose experimental uncertainties are often too large due to limited statistics or large systematics. This situation will drastically change at the LHC, where the statistics and systematics for measurements like the total W, Z, or $t\bar{t}$ cross sections are expected to be reduced to the level of a few percent, comparable to the theoretical accuracy. These and other measurements will allow us to stress-test our modeling of basic phenomena at the LHC, laying the foundations for a successful exploration of the new landscapes that will be uncovered at the energy frontier.

References

1. Feynman R P *Photon–Hadron Interactions* (Reading, Mass.: W.A. Benjamin, 1972)
2. Gross D J *Nucl. Phys. B Proc. Suppl.* **74** 426 (1999); hep-th/9809060; 't Hooft G *Nucl. Phys. B Proc. Suppl.* **74** 413 (1999); hep-th/9808154
3. Muta T *Foundations of Quantum Chromodynamics: An Introduction to Perturbative Methods in Gauge Theories* (Singapore: World Scientific, 1998)
4. Peskin M E, Schroeder D V *An Introduction to Quantum Field Theory* (Reading, Mass.: Addison-Wesley, 1995)
5. Barger V D, Phillips R J N *Collider Physics* (Reading, Mass.: Addison-Wesley, 1997)
6. Ellis R K, Stirling W J, Webber B R *QCD and Collider Physics* (Cambridge: Cambridge Univ. Press, 1996)
7. Campbell J M, Huston J W, Stirling W J *Rep. Prog. Phys.* **70** 89 (2007); hep-ph/0611148
8. Field R D *Applications of Perturbative QCD* (Redwood City, Calif.: Addison-Wesley, 1989)
9. Dokshitzer Yu L et al. *Basics of Perturbative QCD* (Ed. J Tran Thanh Van) (Gif-sur-Yvette Calif.: Editions Frontières, 1991)
10. Dixon L J, arXiv:0712.3064

11. Dobbs M A et al., hep-ph/0403045
12. Gribov V N, Lipatov L N *Yad. Fiz.* **15** 781 (1972) [*Sov. J. Nucl. Phys.* **15** 438 (1972)]
13. Altarelli G, Parisi G *Nucl. Phys. B* **126** 298 (1977)
14. Dokshitzer Yu L *Zh. Eksp. Teor. Fiz.* **73** 1216 (1977) [*Sov. Phys. JETP* **46** 641 (1977)
15. Dittmar M et al., arXiv:0901.2504
16. Jung H et al., arXiv:0903.3861
17. Nadolsky P M et al. *Phys. Rev. D* **78** 013004 (2008); arXiv:0802.0007
18. Martin A D et al. *Eur. Phys. J. C* **63** 189 (2009); arXiv:0901.0002
19. Alekhin S, Melnikov K, Petriello F *Phys. Rev. D* **74** 054033 (2006); hep-ph/0606237
20. Ball R D et al. (NNPDF Collab.) *Nucl. Phys. B* **809** 1 (2009); **816** 293 (2009), erratum; arXiv:0808.1231
21. Reisert B C (H1 and ZEUS Collab.), arXiv:0809.4946
22. Pumplin J et al. *JHEP* (07) 012 (2002); hep-ph/0201195
23. Dokshitzer Yu L et al. *Rev. Mod. Phys.* **60** 373 (1988)
24. Webber B R *Nucl. Phys. B* **238** 492 (1984)
25. Marchesini G, Webber B R *Nucl. Phys. B* **310** 461 (1988)
26. Corcella G et al. *JHEP* (01) 010 (2001); hep-ph/0011363
27. Andersson B et al. *Phys. Rep.* **97** 31 (1983)
28. Sjöstrand T et al. *Comput. Phys. Commun.* **135** 238 (2001); hep-ph/0010017
29. Sjöstrand T, Mrenna S, Skands P *JHEP* (05) 026 (2006); hep-ph/0603175
30. Gieseke S et al. *JHEP* (02) 005 (2004); hep-ph/0311208
31. Melnikov K, Petriello F *Phys. Rev. D* **74** 114017 (2006); hep-ph/0609070
32. Halkiadakis E (for the CDF and D0 Collab.), presented at the Results and Perspectives in Particles Physics: 2009 Rencontres de Physique de la Vallée d'Aoste, La Thuile, Italy, 2009
33. Abazov V M et al. (CDF Collab. and D0 Collab.) *Phys. Rev. D* **70** 092008 (2004); hep-ex/0311039
34. Aaltonen T et al. (CDF Collab.) *Phys. Rev. Lett.* **100** 071801 (2008); arXiv:0710.4112
35. (CDF and D0 Collab.), arXiv:0808.0147
36. The CDF Collab. "Direct measurement of W boson charge asymmetry with 1 fb^{-1} of Run II data", CDF public note 8942, http://www-cdf.fnal.gov/physics/ewk/2007/WChargeAsym/PubNote.pdf
37. Eichten E, Lane K D, Peskin M E *Phys. Rev. Lett.* **50** 811 (1983)
38. Abe F et al. (CDF Collab.) *Phys. Rev. Lett.* **77** 438 (1996); hep-ex/9601008
39. Abbott B et al. (D0 Collab.) *Phys. Rev. Lett.* **86** 1707 (2001); hep-ex/0011036
40. Lai H L et al. *Phys. Rev. D* **55** 1280 (1997); hep-ph/9606399
41. Aaltonen T et al. (CDF Collab.) *Phys. Rev. D* **78** 052006 (2008); arXiv:0807.2204
42. Abazov V M et al. (D0 Collab.) *Phys. Rev. Lett.* **101** 062001 (2008); arXiv:0802.2400
43. Plager C (CDF and D0 Collab.) *Nucl. Phys. B Proc. Suppl.* **186** 407 (2009)
44. Abazov V M et al. (D0 Collab.) *Phys. Rev. D* **80** 071102(R) (2009); arXiv:0903.5525
45. Bonciani R et al. *Nucl. Phys. B* **529** 424 (1998); Cacciari M et al. *JHEP* (04) 068 (2004)
46. Moch S, Uwer P *Phys. Rev. D* **78** 034003 (2008); arXiv:0804.1476
47. Cacciari M et al. *JHEP* (09) 127 (2008); arXiv:0804.2800
48. Kidonakis N, Vogt R *Phys. Rev. D* **78** 074005 (2008); arXiv:0805.3844
49. Frixione S, Ridolfi G, Nason P *JHEP* (09) 126 (2007); Frixione S, Nason P, Webber B R *JHEP* (08) 007 (2003)
50. Mangano M L et al. *JHEP* (01) 013 (2007)
51. Campbell J, Ellis R K *Phys. Rev. D* **65** 113007 (2002); Campbell J, Ellis R K, Rainwater D *Phys. Rev. D* **68** 094021 (2003); hep-ph/0308195
52. Aaltonen T et al. (CDF Collab.) *Phys. Rev. Lett.* **100** 102001 (2008); arXiv:0711.3717
53. Abazov V M et al. (D0 Collab.) *Phys. Lett. B* **658** 112 (2008)
54. Aaltonen T et al. (CDF Collab) *Phys. Rev. D* **77** 011108(R) (2008); arXiv:0711.4044
55. Mangano M L et al. *JHEP* (07) 001 (2003)
56. Mrenna S, Richardson P *JHEP* (05) 040 (2004)
57. Alwall J et al. *Eur. Phys. J. C* **53** 473 (2008)
58. Krauss F et al. *Phys. Rev. D* **70** 114009 (2004); *Phys. Rev. D* **72** 054017 (2005)
59. Lavesson N, Lönnblad N *JHEP* (07) 054 (2005)
60. Maltoni F, Stelzer T *JHEP* (07) 027 (2003)
61. Papadopoulos C G, Worek M *Eur. Phys. J. C* **50** 843 (2007)